TECHNISCHE UNIVERSITÄT WIEN
Vienna University of Technology

MEDICAL UNIVERSITY OF VIENNA

DIPLOMARBEIT

Stimulus selection in functional magnetic resonance imaging based retinotopic mapping

zur Erlangung des akademischen Grades

Diplom-Ingenieur

im Rahmen des Studiums

Technische Physik

eingereicht von

David Linhardt
Matrikelnummer 1325459

ausgeführt am Atominstitut
der Fakultät für Physik der Technischen Universität Wien
in Zusammenarbeit mit dem Institut für Medizinische Physik und Biomedizinische Technik
der Medizinischen Universität Wien

Betreuung
Betreuer: Em.Univ.Prof. Dipl.-Ing. Dr.techn. Gerald Badurek
Betreuer: Assoc. Prof. Priv.-Doz. Dipl.-Ing. Dr. Christian Windischberger
Mitwirkung: Ass.Prof. Dipl.-Ing. Dr.techn. Karin Poljanc

Wien, 5.2.2020

(Unterschrift Verfasser/in) (Unterschrift Betreuer/in)

Die approbierte gedruckte Originalversion dieser Diplomarbeit ist an der TU Wien Bibliothek verfügbar.
The approved original version of this thesis is available in print at TU Wien Bibliothek.
TU Bibliothek Your knowledge hub WIEN

Abstract

For the last 30 years, blood oxygenation level dependent functional magnetic resonance imaging (BOLD-fMRI) has allowed for non-invasive assessment of human brain activity. BOLD-fMRI is based on magnetic susceptibility differences between deoxygenated and oxygenated haemoglobin. In a typical fMRI experiment, series of fast MR images are acquired while stimuli are presented or applied. Sensitivity benefits at ultra-high fields (7 Tesla and above) enable spatial resolutions in the sub-millimetre range. The haemodynamic response function (HRF) describes the change of fMRI signals, which can be associated with neural activity and is used for the analysis of the acquired fMRI time series.

Population receptive field (pRF) mapping is a specific variant of retinotopic mapping, which uses fMRI to assign areas within the primary visual cortex to specific stimulated regions in the visual field. These subject-specific mappingsare typically based on stimuli where differently shaped flickering checkerboards move across the visual field. While pRF mapping experiments have now been carried out for over a decade, there is no consensus on the optimum visual stimuli to be used. The two most commonly used stimuli in state-of-the-art pRF mapping are based on the original publications introducing retinotopic and pRF mapping: the classic "wedges and rings" stimulus by S.A. Engel [1], and the "travelling bar" stimulus by S. O. Dumoulin and B. A. Wandell [2].

In this thesis, these two stimuli variants were compared using 7T fMRI experiments in 10 young, healthy subjects. Data were subjected to pRF-mapping analysis in order to obtain eccentricity and polar angle maps for the reconstruction of visual coverage maps. Here we show that the choice of the visual stimulus variant has substantial effects on the outcome of pRF analysis. In order to further improve the results and profit from the advantages of both stimuli, a novel combination method is introduced and tested.

Die approbierte gedruckte Originalversion dieser Diplomarbeit ist an der TU Wien Bibliothek verfügbar.
The approved original version of this thesis is available in print at TU Wien Bibliothek.
TU Bibliothek Your knowledge hub WIEN

Zusammenfassung

In den vergangen 30 Jahren eröffnete die Technik der Blutoxigenierungsabhängigen funktionellen Magnetresonanztomographie (BOLD-fMRT) die Möglichkeit zur nicht-invasiven Abbildung menschlicher Hirnaktivität. Dieser Effekt basiert auf einer Suszeptibilitätsänderung zwischen oxigeniertem und desoxigeniertem Blut. Bei einem typischen fMRT Experiment werden dem Probanden Stimuli während der Datenaufnahme präsentiert, um gezielt Hirnaktivität auszulösen. Diese Aktivität kann, verzögert durch die hämodynamische Antwortfunktion, aus den fMRT Daten extrahiert werden. Ultra-hohe Magnetfeldstärken (7T und darüber) ermöglichen aufgrund einer Steigerung der Sensitivität Hirnaktivierungskarten mit Auflösungen im sub-Millimeter Bereich.

Bei der Auswertung mittels population receptive field (pRF) mapping wird eine Karte erstellt, welche jedem Punkt auf dem Kortex eindeutig einen Bereich im visuellen Feld zuordnet. Um das zu erreichen, werden bei der Messung flackernde Schachbrettmuster gezeigt, die sich in bestimmten Konfigurationen durch das Gesichtsfeld bewegen. Die beiden meist genutzten Stimuli sind einerseits rotierende Kreissegmente, kombiniert mit sich erweiternden bzw. verengenden Ringen, und andererseits Balken, welche in verschiedenen Richtungen durch das Gesichtsfeld wandern. Obwohl die pRF Methode seit bereits über einem Jahrzehnt angewandt wird, gibt es bis heute keinen Konsens, welche Stimulusvariante zu optimalen Ergebnissen führt.

Es werden die beiden konventionellen Stimuli anhand von Daten von 10 jungen, gesunden Versuchspersonen verglichen, welche an einem 7T Retinotopie-Experiment teilgenommen haben. Mit Hilfe der pRF Analyse werden Exzentrizitäts- und Polarwinkel-Karten erstellt, um auf die personenspezifische Abdeckung des visuellen Blickfeldes rückzuschließen. Es wird gezeigt, dass die Wahl des Stimulus beträchtlichen Einfluss auf das Ergebnis der pRF Analyse hat. Weiters wird eine neue Art der Kombination der verschiedenen Stimuli vorgestellt, die die Vorteile beider Varianten bündelt.

Die approbierte gedruckte Originalversion dieser Diplomarbeit ist an der TU Wien Bibliothek verfügbar.
The approved original version of this thesis is available in print at TU Wien Bibliothek.
TU Bibliothek Your knowledge hub WIEN

Contents

Die approbierte gedruckte Originalversion dieser Diplomarbeit ist an der TU Wien Bibliothek verfügbar.
The approved original version of this thesis is available in print at TU Wien Bibliothek.
TU Bibliothek Your knowledge hub WIEN

Die approbierte gedruckte Originalversion dieser Diplomarbeit ist an der TU Wien Bibliothek verfügbar.
The approved original version of this thesis is available in print at TU Wien Bibliothek.
TU Bibliothek Your knowledge hub WIEN

1 Introduction

Paul Christian Lauterbur [3] and Peter Mansfield [4] introduced nuclear magnetic resonance (NMR) imaging in the 1970s, based on previous work from Felix Bloch [5] and Edward Mills Purcell [6] in the 1940s, who independently discovered the phenomena of NMR. Today, besides chemical analysis, where NMR is used to assess details of the electronic structure of a molecule, and it is individual functional groups, the main application of NMR is in magnetic resonance imaging (MRI), used in clinical diagnosis and research, since the technique allows for high-resolution in-vivo examinations free from ionising radiation.

An essential step in the evolution of MRI was the introduction of functional MRI (fMRI) by Ogawa et al. in 1990 [7], based on the blood-oxygenation level dependent (BOLD) effect. This effect is based on the fact that firing neurons increase oxygen consumption in task-related areas. Importantly, local blood oxygenation level is not reduced but increased due to increased inflow of arterial blood, which overcompensates oxygen consumption. Based on the different magnetic properties of oxygenated and deoxygenated blood, MRI signal amplitudes change in the percent range. This fact enables the non-invasive investigation of task-related neuronal activation. As the BOLD-fMRI mechanism relies on changes in blood flow, MRI signal changes are delayed by a several seconds. This is referred to as the haemodynamic response function (HRF) and has to be taken into account for analysis.

Numerous brain regions have been targeted by fMRI research so far. The research field investigating the mapping of visual input from the retina to the visual cortex is referred to as retinotopy or retinotopic mapping. In a modern variant of retinotopic mapping, so-called population receptive field (pRF) mapping, the aim is to find subject-specific correlations between areas on the visual cortex and the subject's field of view. This goal is achieved by presenting stimuli of flickering checkerboard shapes moving through the visual field. Simultaneously, high-resolution images of the primary visual cortex (V1) are

Die approbierte gedruckte Originalversion dieser Diplomarbeit ist an der TU Wien Bibliothek verfügbar.
The approved original version of this thesis is available in print at TU Wien Bibliothek.
TU Bibliothek Your knowledge hub WIEN

acquired every second. The two most common stimuli, the so-called "travelling bar" and "wedges and rings", are based on the works of S.A. Engel [1] in 1994 and S. O. Dumoulin and B. A. Wandell [2] in 2008. However, although these stimuli have been introduced over a decade ago, there is still no consensus about the optimal stimulus. After the acquisition, images have to go through a pre-processing in multiple stages in order to compensate for, e.g. patient movement or artefacts caused by small field inhomogeneities. The following analysis tries to find the corresponding position on the visual field, for every part in the visual cortex, based on the recorded activations on the cortex. Additionally, a high-resolution anatomical image is recorded to perform a segmentation into white and grey matter.

This thesis starts with a brief introduction to the basics of MRI and fMRI in chapter 2, the human visual system in chapter 3 and retinotopic mapping in chapter 4. Following this, in chapter 5, an experiment is described where the method of retinotopic mapping was used in an ultra-high field MRI scanner (7T Siemens MAGNETOM) on ten young, healthy subjects in order to acquire representative data. Different stimuli are used for later comparison. Eccentricity and polar angle maps, as well as visual field coverage maps, are made after the pRF analysis. It will be shown that the choice of the visual stimulus variant has considerable effects on the pRF analysis results. In order to utilise both stimulus advantages, a novel combination method is introduced and tested.

Die approbierte gedruckte Originalversion dieser Diplomarbeit ist an der TU Wien Bibliothek verfügbar.
The approved original version of this thesis is available in print at TU Wien Bibliothek.
TU Bibliothek Your knowledge hub WIEN

2 Nuclear Magnetic Resonance

The phenomena of nuclear magnetic resonance (NMR) were introduced independently by Felix Bloch [5] and Edward Mills Purcell [6] in 1946. Both researchers shared the Nobel Prize in Physics in 1952. During the following years, NMR was used almost exclusively for chemical analysis. The basic concepts of imaging based on NMR were presented by Paul Christian Lauterbur [3] and Peter Mansfield [4] in the early 1970s. These ideas have laid the basis for the immense importance of magnetic resonance imaging (MRI) in clinical diagnosis and research today. In recognition of their efforts, they were awarded the Nobel Prize in Physiology or Medicine in 2003.

The following is a short introduction to the physical principles underlying nuclear magnetic resonance and magnetic resonance imaging, based on [8].

2.1 Physical background

NMR is based on manipulating nuclear magnetic moments. Thus, NMR can only be applied to isotopes with non-zero nuclear spin. Due to the high presence of water in the human body, the single proton in the nucleus of ^1H hydrogen is an ideal target. Using models from classical physics the magnetic moment (spin) of this proton will precess when placed in an external magnetic field $\vec{B}_0$ as seen in Figure 2.1.

The frequency of this precession is named Larmor frequency ω_0 and is given by

$$\omega_0 = -\gamma B_0 \tag{2.1}$$

where γ is the gyromagnetic factor, a particle-specific constant. The hydrogen nucleus has a gyromagnetic factor of around 2.68×10^8 rad/(s T). In 3 T and 7 T NMR scanners it will, therefore, precess at with a rotation frequency of around 123.1 MHz and 297.2 MHz, respectively.

Die approbierte gedruckte Originalversion dieser Diplomarbeit ist an der TU Wien Bibliothek verfügbar.
The approved original version of this thesis is available in print at TU Wien Bibliothek.
TU Bibliothek Your knowledge hub WIEN

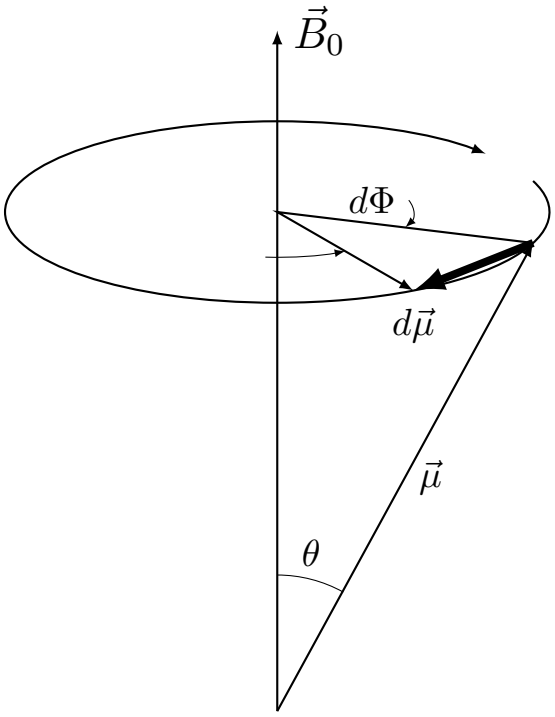

Figure 2.1: Precession of the spin with a dipole moment $\vec{\mu}$ around the external magnetic field $\vec{B}_0$

Switching to quantum mechanics, we may state that a spin-$\frac{1}{2}$ particle (like the proton) will have two possible orientations when exposed to an external magnetic field: parallel or anti-parallel to the field. These two orientations represent different energy levels ($|+\frac{1}{2}\rangle$, $|-\frac{1}{2}\rangle$) in the proton's spectral lines. The spectral line splitting due to an external magnetic field is called the Zeeman effect.

The energy of a sppin μ in an external magnetic field B_0 is given as

$$E = -\mu_z B_0 \tag{2.2}$$

with the magnetic moment

$$\mu_z = g_p \frac{q_e}{2m_p} J_z \tag{2.3}$$

where g_p refers to the nuclear g-factor (5.59 for protons) and q_e to the electron charge Discrete energy values can be generally calculated as

$$E = -g_p \mu_N B_0 \frac{J_z}{\hbar} \tag{2.4}$$

Die approbierte gedruckte Originalversion dieser Diplomarbeit ist an der TU Wien Bibliothek verfügbar.
The approved original version of this thesis is available in print at TU Wien Bibliothek.
TU Bibliothek Your knowledge hub WIEN

The nuclear magneton $\mu_N = \frac{q_e \hbar}{2m_p}$ is introduced here for simplification. The two possible energy levels for corresponding to the spin states $\frac{J_z}{\hbar} = \pm\frac{1}{2}$ simplify to

$$E_{\pm\frac{1}{2}} = \pm\frac{1}{2} g_p \mu_N B_0 \tag{2.5}$$

and the energy difference is

$$\Delta E = g_p \mu_N B_0 \tag{2.6}$$

Population densities of the two states follow the Boltzmann distribution

$$p(E_i) = \frac{e^{-E_i/kT}}{\sum_{j=1}^{N} e^{-E_j/k_B T}} \tag{2.7}$$

where $E_\pm$ to the energy of the two states, N is the total number of possible states, T is the system's absolute temperature and k_b the Boltzmann-constant. In case of in-vivo MRI, T is equal to the body temperature. Since the parallel $|+\frac{1}{2}\rangle$ state represents a lower energy level than the anti-parallel $|-\frac{1}{2}\rangle$ state the energy levels can be compared:

$$\frac{p(E_{+\frac{1}{2}})}{p(E_{-\frac{1}{2}})} = e^{\frac{\Delta E}{k_B T}} \tag{2.8}$$

At 3 T magnetic field strength the difference in a population of $N = 2 \times 10^5$ is only a single spin . Due to the fact that even 1 mL of water contains around 6.7×10^{22} hydrogen nuclei, it is still possible to measure a signal despite the small population difference.

As modelling the basic phenomena of an MRI experiment can be accomplished without the use of extensive quantum mechanical equations, we now focus on a semi-classic description. We here assume that the summation over all spins inside the volume considered yields a total magnetisation vector $\vec{M}_0$ in the direction of the external magnetic field. The amplitude of M_0 is dependent on the population difference and the total number of spins N and can be defined as

$$M_0 = N(p(E_{+\frac{1}{2}})\mu_{z,+\frac{1}{2}} + p(E_{\frac{1}{2}})\mu_{z,-\frac{1}{2}}) \tag{2.9}$$

Die approbierte gedruckte Originalversion dieser Diplomarbeit ist an der TU Wien Bibliothek verfügbar.
The approved original version of this thesis is available in print at TU Wien Bibliothek.
TU Bibliothek Your knowledge hub WIEN

Since the nuclear magnetic energies ar much smaller than the thermal energies ($E \ll k_B T$) it can be simplified with the help of the exponential power series ($e^a = 1 + a + \mathcal{O}(a^2)$):

$$M_0 \approx \frac{1}{4} N \frac{\gamma^2 \hbar^2}{k_B T} B_0 \tag{2.10}$$

It can be seen, that higher magnetic field will result in higher population differences and thus greater magnetization vector amplitudes.

Following Faraday's law of induction, a varying magnetic field can induce voltages in a coil. In order to measure the induced signal in the receive coils, the total magnetisation vector $\vec{M}$ needs to perform a precession movement around the $\vec{B}_0$ field. This precession movement is described in the so-called Bloch equations, further discussed in section 2.3. The precession is forced by flipping $\vec{M}$ into the xy-plane by application of a radio-frequency pulse $\vec{B}_1$ in transversal direction. Flipping around $\vec{B}_1$ corresponds to the precession movement of magnetic moments in magnetic fields. In Figure 2.2, the radio-frequency pulse is represented by $\vec{B}_1$ in the rotating frame of reference. Magnetisation starting at $\vec{M}(0)$, begins to precess around the pulsed magnetic field $\vec{B}_1$ and reaches its final orientation $\vec{M}$ when the rf-pulse is stopped. The flipping angle $\Delta\Theta$ (Figure 2.2) is depending on the rf-pulse amplitude B_1 and pulse duration t_p, as

$$\Delta\Theta = \gamma B_1 * t_p \tag{2.11}$$

It is further essential that the rf-pulse is applied with the hydrogens resonance frequency ω_0 at the corresponding static magnetic field $\vec{B}_0$ for an efficient flipping of the magnetisation vector. This resonance frequency lies within the radio-frequency domain. Hence it is referred to as radio-frequency (rf) pulse.

In order to simplify the description of the magnetisation vector precession movement, a transition to a rotating coordinate system is performed. These primed axes represent the coordinate system rotating with Lamor frequency around the z'-axis. Now the magnetisation vector $\vec{M}$ itself in the equilibrium, non-exited condition is static.

After flipping $\vec{M}$ into the $x'y'$-plane, the resulting rotation of $\vec{M}$ induces a voltage and therefore a signal in nearby receive coils. The total signal measured in an NMR experiment is proportional to the square of the magnetic field as well as the temperature (2.12). As the body temperature (T) cannot be manipulated for in vivo experiments, the

Die approbierte gedruckte Originalversion dieser Diplomarbeit ist an der TU Wien Bibliothek verfügbar.
The approved original version of this thesis is available in print at TU Wien Bibliothek.
TU Bibliothek Your knowledge hub WIEN

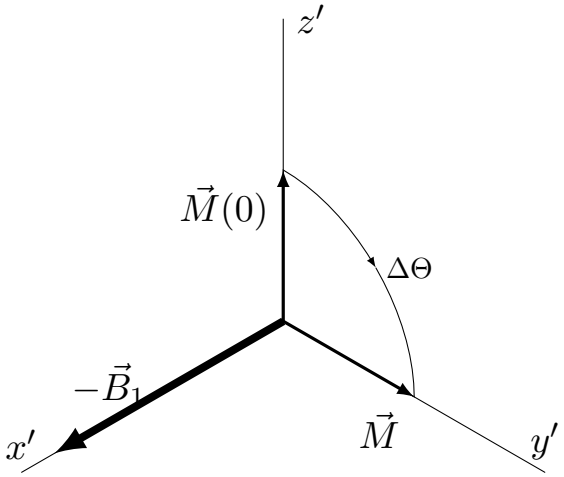

Figure 2.2: Flip of the magnetisation $\vec{M}$ into the $x'y'$-plane by a radio-frequency magnetic field pulse in x' direction

only way to increase signal amplitude is by performing the scan at higher magnetic field strengths (B_0).

$$signal \propto \frac{\gamma^3 B_0^2 \rho_0}{T} \tag{2.12}$$

2.2 NMR relaxation and sequences

The contrast of an NMR signal depends on spin density, substance-specific relaxation constants tied to longitudinal relaxation T_1 (spin-lattice relaxation), transverse relaxation T_2 (spin-spin relaxation) as well as on a sequence of radio frequency (rf) fields, which can be characterised by repetition time (TR) and echo time (TE). In the following, these parameters will be introduced by discussing three exemplary rf-pulse sequence types.

2.2.1 Free Induction Decay and $T_2^\star$

Free induction decay (FID) is the most straightforward MR experiment where the magnetisation is rotated into the $x'y'$-plane by a $\frac{\pi}{2}$-pulse. The measured signal decays exponentially, characterised by time constant $T_2^\star$. After application of the rf-pulse, spins are still aligned, performing a precession movement around the main magnetic field $\vec{B}_0$. As their magnetic fields interact with each other, phase coherence is gradually lost, leading

Die approbierte gedruckte Originalversion dieser Diplomarbeit ist an der TU Wien Bibliothek verfügbar.
The approved original version of this thesis is available in print at TU Wien Bibliothek.

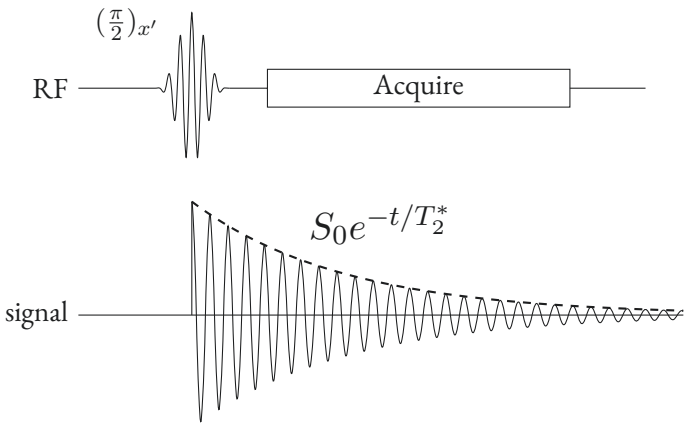

Figure 2.3: Free induction decay of the magnetisation after an $\frac{\pi}{2}$-pulse in the rotating frame of reference

to the decay of the transverse magnetisation component. Time constant $T_2^\star$ includes two dephasing components: spin-spin interaction and field inhomogeneities. Both can be modelled by separate decay constants T_2 and T_2', respectively. These two decay mechanisms are combined as $\frac{1}{T_2^\star} = \frac{1}{T_2} + \frac{1}{T_2'}$ and therefore the resulting time constant $T_2^\star$ is significantly smaller than T_2.

2.2.2 Spin Echo Sequence and T_2

Spin-echo sequences employ an additional π-pulse to compensate effects of B_0 inhomogeneities and can be used to determine the T_2 constant. This sequence type (Figure 2.4) is based on two rf pulses, a $\frac{\pi}{2}$ excitation pulse, and a π refocusing pulse. The echo time T_E, i.e. the time between the excitation and signal detection, is twice the time τ between the two pulses $T_E := 2\tau$.

The spin-echo procedure may be described in three steps, as illustrated in Figure 2.5. In the first step, the $\frac{\pi}{2}$ excitement-pulse is applied along the direction of the x'-axis and the magnetisation vector $\vec{M}$ flips to the $x'y'$-plane. After this flip, $\vec{M}$ precesses around the main magnetic field B_0 in z-direction. Due to local inhomogeneities, spins at different locations precess at slightly different frequencies, leading to spin dephasing and subsequent reduction in MR signal amplitude. The second rf-pulse is a π-pulse applied after time τ, along the y'-axis which inverts the phase of the spins. As long as spins stay at the same physical location, they preserve their precession speed and realign in phase

Die approbierte gedruckte Originalversion dieser Diplomarbeit ist an der TU Wien Bibliothek verfügbar.
The approved original version of this thesis is available in print at TU Wien Bibliothek.

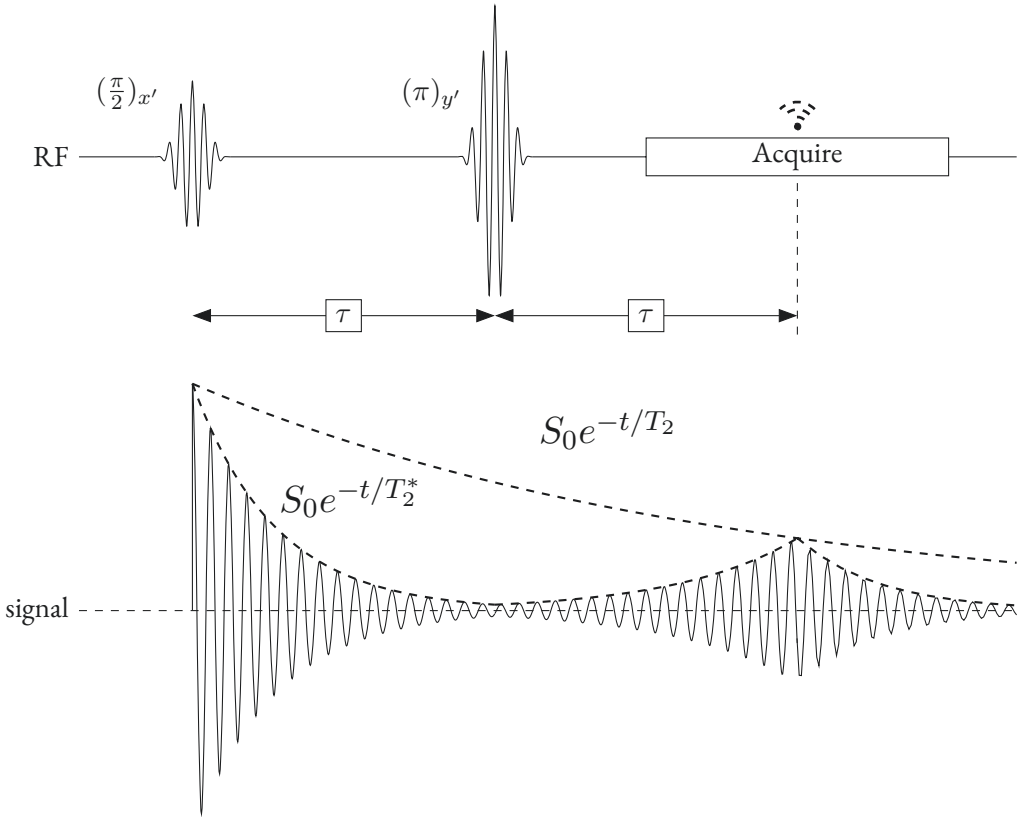

Figure 2.4: Spin Echo sequence and the measured signal in the rotating laboratory frame for the measurement of T_2. The schematic movement of the magnetisation vector can be seen in Figure 2.5.

Die approbierte gedruckte Originalversion dieser Diplomarbeit ist an der TU Wien Bibliothek verfügbar.
The approved original version of this thesis is available in print at TU Wien Bibliothek.

after time τ. This reestablished phase coherence results in a signal maximum at the echo time $TE = 2\tau$ after the initial 90° pulse, which is referred to as spin echo (Figure 2.4). The enveloping function is represented by an exponential decay characterised by the time constant T_2. The π-pulse can be applied repeatedly to obtain additional spin echoes.

2.2.3 Inversion Recovery and T_1

Beside methods where the tissue-specific parameters T_2 and $T_2^\star$ are time constants describing the decay of the transversal component M_{xy} of the magnetisation vector $\vec{M}$, the longitudinal component M_z also shows relaxation behaviour. This return to thermal equilibrium conditions is characterized by the longitudinal relaxation constant T_1. It is important to note that transversal and longitudinal relaxation are two independent processes. While excitation may be seen as a spiral-like trajectory of $\vec{M}$, relaxation represents a decrease of the transversal component via spin dephasing and an increase of the longitudinal component via energy exchange between spins their environment ("lattice").

The inversion recovery (IR) method can be used for measuring longitudinal relaxation and the corresponding time constant T_1. In an IR sequence, a π-pulse is applied initially to invert the thermal equilibrium magnetization vector from $+z'$ to $-z'$ direction. Subsequently, the system will progress towards baseline conditions; thus, the magnetisation will relax back to its initial direction along the z'-axis. After time T_I, M_z is flipped into the $x'y'$-plane and a signal proportional to the absolute value of M_z is measured.

The time between the initial π and the following $\frac{\pi}{2}$ pulse for excitation is defined as inversion time T_I. Between the two pulses, the spins undergo T_1 relaxation. By repeating these steps for several different inversion times, the longitudinal relaxation process may be covered, and the specific time-constant T_1 calculated. In some imaging applications, it is beneficial to suppress ("null") signal from a specific tissue (e.g. fat). This can be achieved by setting inversion time to $T_{I,null} = T_{1,null} ln2$, given that $T_{1,null} \ll TR$. As magnetisation of the target tissue will pass zero at $T_{I,null}$, this tissue type will not be visible in the images acquired. Figure 2.6 shows the absolute value of the magnetisation $\mathbf{M}$ as function of the inversion time T_I.

Die approbierte gedruckte Originalversion dieser Diplomarbeit ist an der TU Wien Bibliothek verfügbar.
The approved original version of this thesis is available in print at TU Wien Bibliothek.
TU Bibliothek Your knowledge hub WIEN

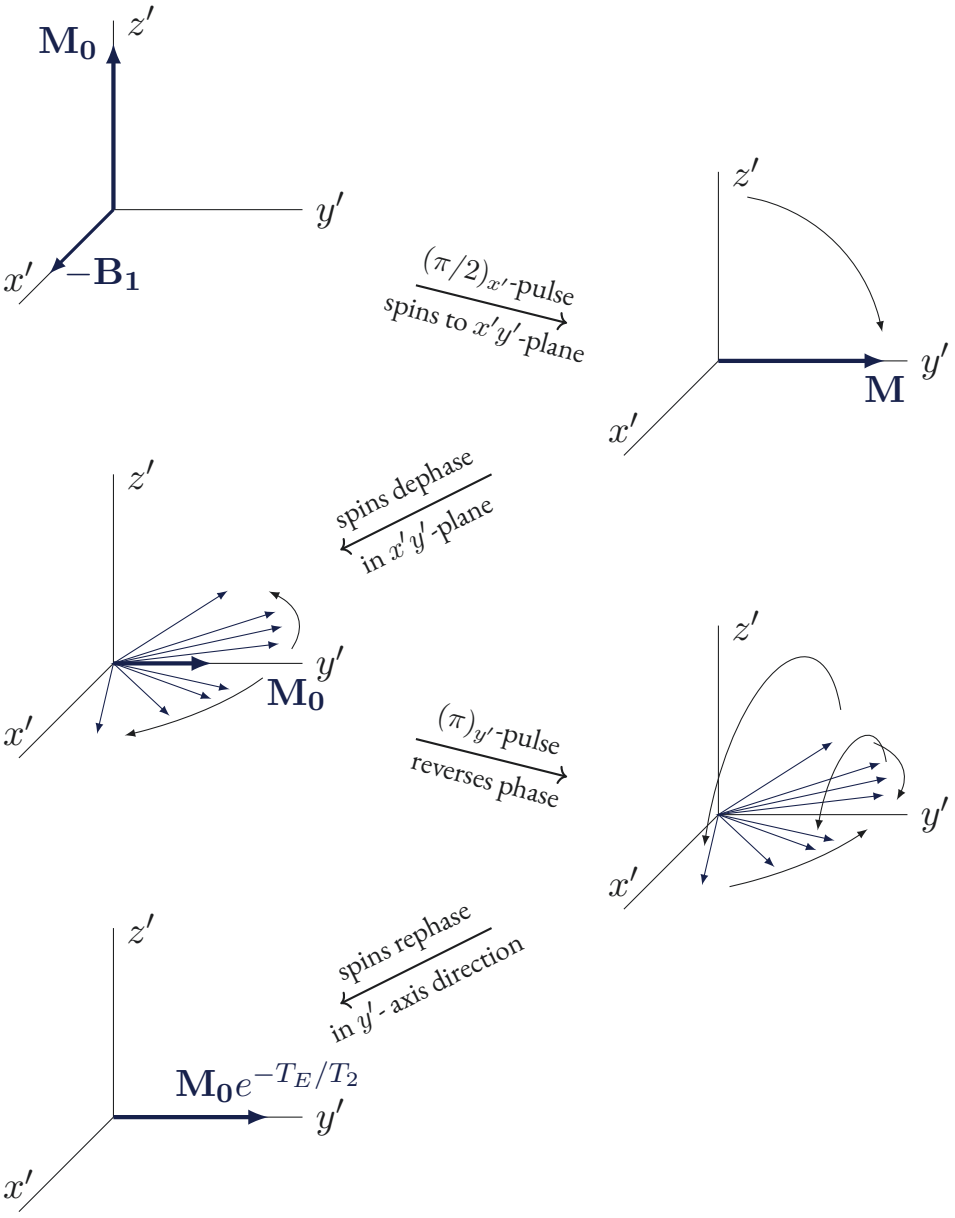

Figure 2.5: Dephasing process of spins after $\frac{\pi}{2}$-pulse followed by rephasing induced by a π-pulse in the rotating frame of reference. Spin sequence and resulting signal can be seen in Figure 2.4.

Die approbierte gedruckte Originalversion dieser Diplomarbeit ist an der TU Wien Bibliothek verfügbar.
The approved original version of this thesis is available in print at TU Wien Bibliothek.

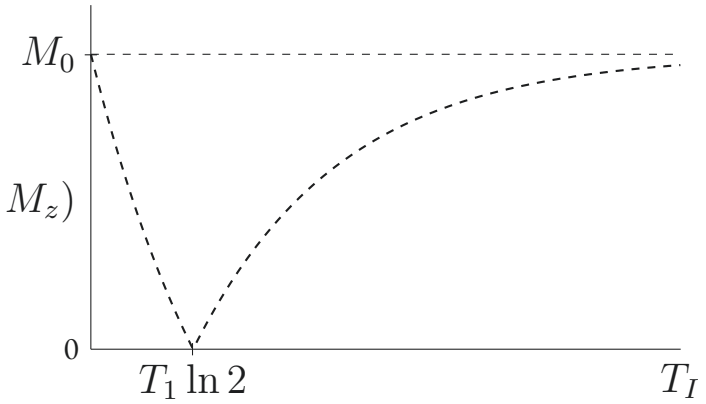

Figure 2.6: Absolute value of the magnetisation M as function of T_I as measured for the evaluation of T_1.

2.3 Bloch equations

The net magnetization vector is formed due to the population difference in an external magnetic field and can be defined as all magnetic moments $\vec{\mu}$ in a defined volume element dV:

$$\vec{M} = \frac{d\vec{\mu}}{dV} \tag{2.13}$$

The system strives to restore minimum energy state which it reaches after relaxation at $M_z = M_0$ and $M_{xy} = 0$, with the z-axis is parallel to the main magnetic field.

The Bloch equations (2.14) are a set of macroscopic equations describing the precession in the external magnetic field, as well as different relaxation processes, dependent on the substance-specific time-constants T_1 and T_2, and therefore the time-course of the net magnetization vector $\vec{M} = (M_x, M_y, M_z)$.

$$M_x(t) = M_x(0)\sin(\omega_L t) - \frac{t}{T_2} \tag{2.14a}$$

$$M_y(t) = M_y(0)\cos(\omega_L t)e^{-\frac{t}{T_2}} \tag{2.14b}$$

$$M_z(t) = M_0 - (M_0 - M_z(0))e^{-\frac{t}{T_1}} \tag{2.14c}$$

While (2.14c) represents the longitudinal magnetisation in field direction, (2.14a) and (2.14b) describe the transverse magnetisation and therefore the precession movement

Die approbierte gedruckte Originalversion dieser Diplomarbeit ist an der TU Wien Bibliothek verfügbar.
The approved original version of this thesis is available in print at TU Wien Bibliothek.
TU Bibliothek Your knowledge hub WIEN

with frequency ω_L around the main magnetic field $\vec{B}_0$. The enveloping function for the transverse magnetisation calculates as

$$M_{xy}(t) = M_{xy}(0)e^{-\frac{t}{T2}} \tag{2.15}$$

For the special case of a $\frac{\pi}{2}$ or 90° pulse, $\vec{M}$ is rotated int he xy-plane and the equation simplifies to

$$M_{xy}(t) = M_0 e^{-\frac{t}{T2}} \tag{2.16a}$$

$$M_z(t) = M_0(1 - e^{-\frac{t}{T1}}) \tag{2.16b}$$

2.4 Magnetic Resonance Imaging

The methods presented so far considered the spin ensemble as a whole. In order to obtain images, i.e. maps of spin distributions weighted by relaxation constants, it is necessary to divide the whole three-dimensional probe into several subparts, the so-called voxels, and encode every voxels information dependent on its spatial position. Key to this necessary encoding is the introduction of additional magnetic gradient fields. This new technique for the acquisition of three-dimensional images is called magnetic resonance imaging (MRI).

2.4.1 Gradient fields

Slice Selection

As a first step in the three-dimensional encoding process, excitation is limited to a single slice of the volume as illustrated in Figure 2.7. This is achieved by applying a linear gradient field in slice direction $G_z(z)$ simultaneously to the initial rf excitation pulse. The superposition of the gradient field and the rf-pulse $\gamma(B_0+G_z(z))$ result in excitation in a small area Δz, since the pulse is off-resonance in other parts of the volume. The thickness of this area, and therefore the selected slice, as well as the position of this area, depends on the chosen rf-pulse bandwidth $\Delta\omega$ and the applied gradient field. In order to compensate for rotation frequency changes due to the slice-selection gradient, a compensation pulse is applied in negative gradient direction.

Die approbierte gedruckte Originalversion dieser Diplomarbeit ist an der TU Wien Bibliothek verfügbar.
The approved original version of this thesis is available in print at TU Wien Bibliothek.
TU Bibliothek Your knowledge hub WIEN

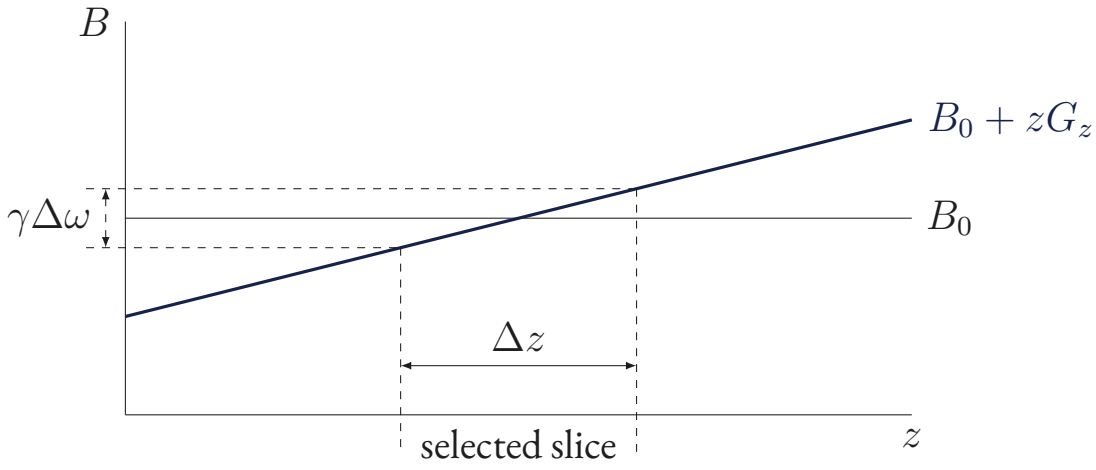

Figure 2.7: The introduction of a gradient field along the z-axis G_z slightly modifies the spin's Larmor frequency depending on the spatial position. This allows for excitation uniquely in the selected area, where resonance condition is met. The excited area depends on the gradient field and the bandwidth of the rf-pulse.

Frequency Encoding

The frequency-encoding step is based on the application on a linear gradient during the signal acquisition. This so-called "readout" gradient alters the strength of the main magnetic field, and therefore the spins precession frequency according to their position along readout direction. Combined with the linear gradient G_x the magnetic field is now location-dependent

$$B(x) = B_0 + xG_x \tag{2.17}$$

and the local Larmor frequency is modified as

$$\omega_L(x) = \gamma B(x) = \omega_0 + \omega_{Gx}(x) \tag{2.18}$$

Due to this shift, the different NMR spectrum frequencies correspond to different spatial positions. The local proton densities can be calculated since the peaks are proportional to the local spin density.

Die approbierte gedruckte Originalversion dieser Diplomarbeit ist an der TU Wien Bibliothek verfügbar.
The approved original version of this thesis is available in print at TU Wien Bibliothek.
TU Bibliothek Your knowledge hub WIEN

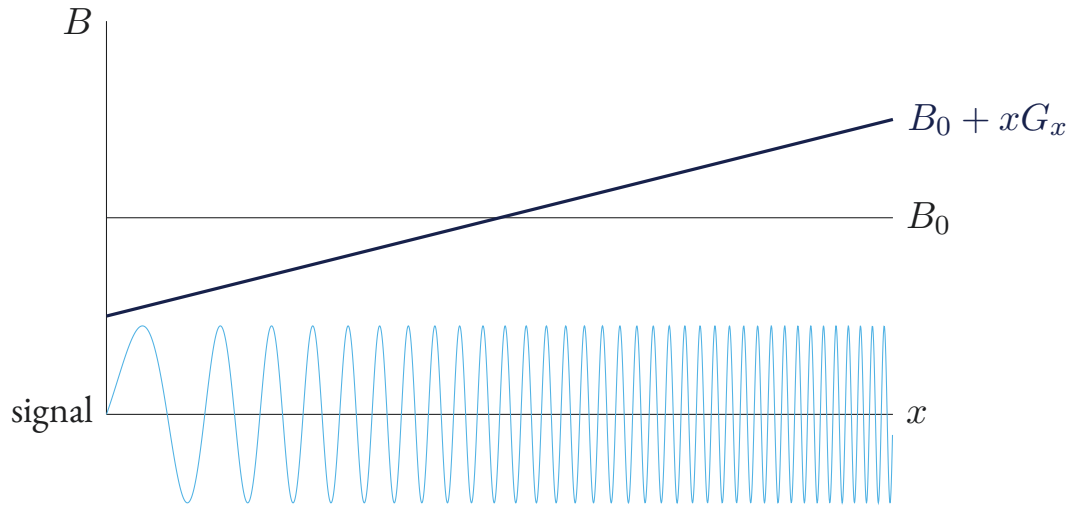

Figure 2.8: The introduced frequency encoding gradient G_x alters the spins rotation frequency dependent on their x position.

Phase Encoding

In order to acquire the second dimension within the selected slice, the so-called "phase-encoding" gradient G_y is introduced. The phase encoding gradient is applied briefly between slice-selection and readout to introduce location-dependent shifts in phase which stay constant throughout the readout process and therefore can be associated with a local phase shift

$$\Delta\Phi = yG_y\Delta t \tag{2.19}$$

To avoid phase-wrapping effects, the phase-encoding gradient step has to be reapplied with different gradient amplitudes in order to produce unique phases for every spatial position. As a consequence, this encoding step has to be repeated once for every voxel in phase-direction.

2.4.2 k-Space and image reconstruction

While the concept of readout and phase-encoding gradients is ideally suited as an introduction to the image encoding procedure, it must be noted that full coverage of the differ-

Die approbierte gedruckte Originalversion dieser Diplomarbeit ist an der TU Wien Bibliothek verfügbar.
The approved original version of this thesis is available in print at TU Wien Bibliothek.
TU Bibliothek Your knowledge hub WIEN

ent encoding aspects may only be achieved by moving into the 2D Fourier-transformed image space, i.e. k-space, where k is defined as

$$k_x(t) = \gamma G_x t \tag{2.20a}$$

$$k_y(t) = \gamma G_y t \tag{2.20b}$$

Using this approach, image acquisition can be re-interpreted as acquiring the signal $S(k_x, k_y)$ throughout k-space. As defined in the equations above, moving through k-space can be achieved by switching gradients G_x and G_y.

k-space has the same dimensions as the image space, but there is no point-to-point mapping between the different domains. Instead, every point on the frequency domain corresponds to a complex number, which contains information about every pixel in the image. The superposition of all k-space information results in the final image. The mathematical operation, for the transformation between image and frequency domain may be achieved by Fourier transformation:

$$S(\vec{k}) \propto \iint s(\vec{r}) e^{-i\vec{k}\vec{r}} d^2r \tag{2.21a}$$

$$s(\vec{r}) \propto \iint S(\vec{k}) e^{i\vec{k}\vec{r}} d^2k \tag{2.21b}$$

(2.21b) is called inverse Fourier transform and leads from the scanner signal $S(\vec{k})$ in the k-space to the image domain $s(\vec{r})$, while (2.21a) represents the inverse process. Here a two-dimensional transformation is shown, but the processes can easily extended to three dimensions. For such 3D acquisition, a third encoding gradient G_z will be required and imaging reconstruction will be perfomed by 3D Fourier transformation.

Due to the specific features of the Fourier transformation, central parts of k-space represent low spatial frequencies and therefore contain information about the contrast of the image, while more peripheral areas, and therefore high spatial frequencies are associated with high spatial resolution features.

In order to acquire an image of a certain matrix size, it is necessary to fill up the same matrix size in the corresponding k-space. A straightforward approach is to papply a short gradient pulse after excitation ot reach a desired k-space line and acquire the data. This is repeated until the whole k-space is covered. This sequence is referred to as "spin-warp"

Die approbierte gedruckte Originalversion dieser Diplomarbeit ist an der TU Wien Bibliothek verfügbar.
The approved original version of this thesis is available in print at TU Wien Bibliothek.
TU Bibliothek Your knowledge hub WIEN

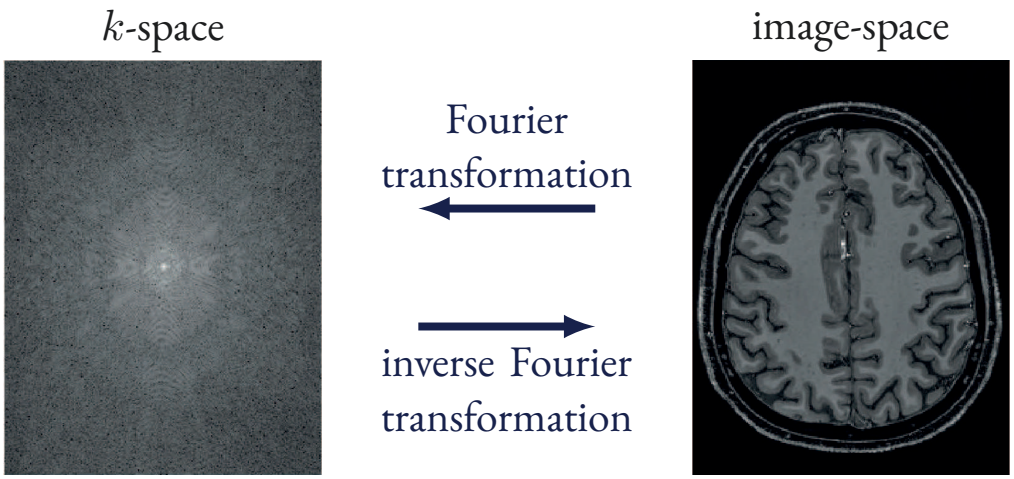

Figure 2.9: On the left hand side, the acquired image in the k-space is shown, which can be transformed to the image space on the right hand side by application of an inverse 2D Fourier transformation.

sequence and is shown in Figure 2.10. Through the variation of the length and strength of the phase encoding gradient, different positions can be accessed. After the k-space is filled, the image can be calculated by applying the inverse 2D Fourier transformation.

Die approbierte gedruckte Originalversion dieser Diplomarbeit ist an der TU Wien Bibliothek verfügbar.
The approved original version of this thesis is available in print at TU Wien Bibliothek.
TU Bibliothek Your knowledge hub WIEN

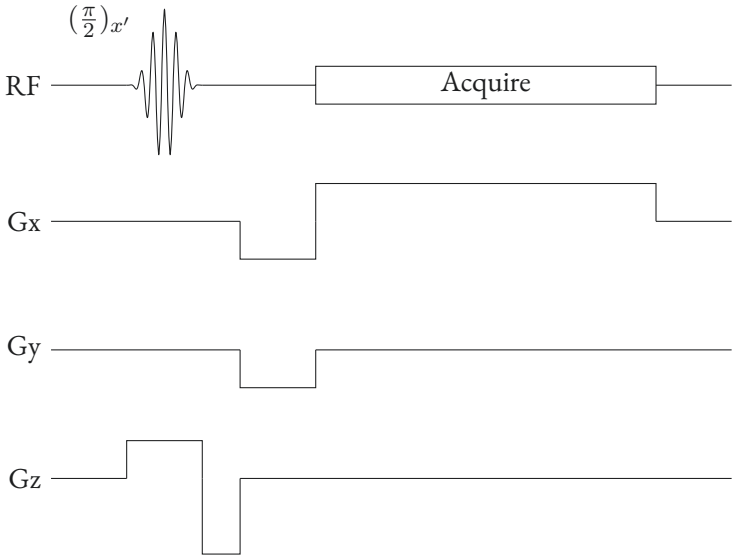

Figure 2.10: This spin-warp sequence uses the G_z gradient while excitation for the selection of an single slice. Further the gradients G_x and Gy_y are used between the rf-pulse and the acquisition in order to navigate to the desired position in k-space. Afterwards the frequency encoding step is performed while acquisition in order to go through the k-space line. This sequence is repeated with different frequency encoding gradients G_y in order to acquire the whole k-space line by line.

2.5 Functional Magnetic Resonance Imaging

First studies showing the correlation between neural activation and Cerebral Blood Flow (CBF) were published at the end of the 19th-century [9], where a patient with a defective skull was investigated. There, pulsation increased when the subject was asked to perform arithmetic calculations.

2.5.1 BOLD Effect

Intuitively one would assume, that the blood oxygenation is reduced in active areas, due to the higher oxygen consumption. However, this is not the case because the higher oxygen usage is overcompensated by an increase in CBF in these areas.Although the reason for this overcompensation in active brain areas is not yet resolved, fMRI would not be possible without this effect. The so-called blood oxygenation dependent (BOLD) effect is based on changing magnetic properties of the haemoglobin molecule when oxygen is delivered by it.

Die approbierte gedruckte Originalversion dieser Diplomarbeit ist an der TU Wien Bibliothek verfügbar.
The approved original version of this thesis is available in print at TU Wien Bibliothek.
TU Bibliothek Your knowledge hub WIEN

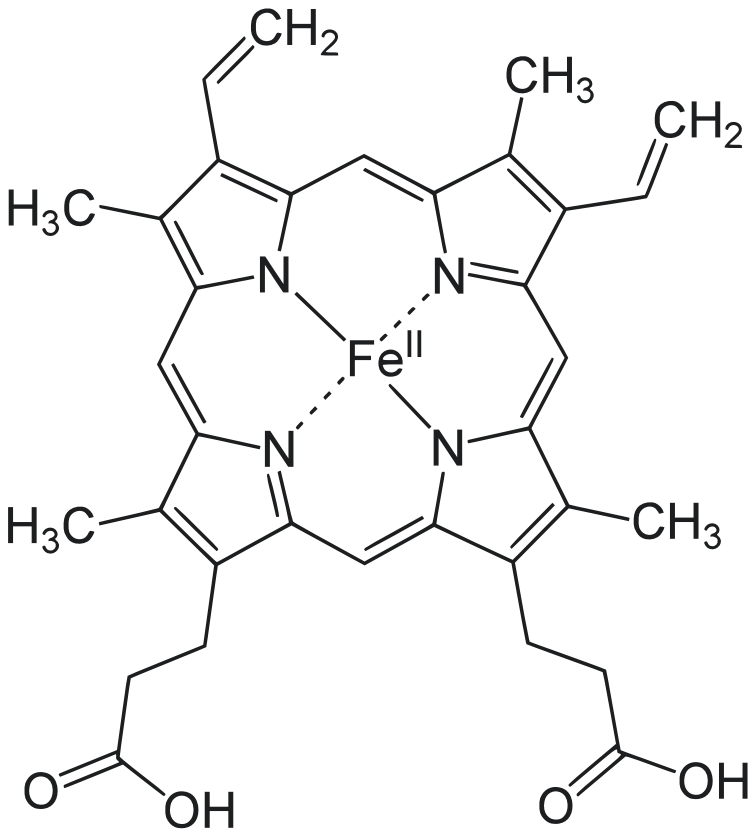

Figure 2.11: Structure of Haemoglobin molecule. The central iron atom is capable of binding oxygen for transportation. [10]

In oxygenated blood, the central iron atom of haemoglobin (Figure 2.11) can be seen as shielded from the surrounding magnetic fields by the bound oxygen atom. This oxyhaemoglobin has no unpaired electrons and is diamagnetic.

After the delivery of the oxygen, the iron atom is less shielded, and there are unpaired electrons in the haemoglobin complex. Therefore, deoxyhaemoglobin is paramagnetic. These properties result in different magnetic susceptibilities of blood in the different oxygenation states and cause changes in the MR signal. The relaxation time constant T_2 decreases quadratically depending on B_0 and deoxyhaemoglobin ratio. Further, $T_2^\star$ constant decreases even more rapidly due to local field inhomogeneities and following precession frequency differences. When performing functional magnetic resonance imaging (fMRI), exactly these effects are used to measure image intensity differences.

Die approbierte gedruckte Originalversion dieser Diplomarbeit ist an der TU Wien Bibliothek verfügbar.
The approved original version of this thesis is available in print at TU Wien Bibliothek.
TU Bibliothek Your knowledge hub WIEN

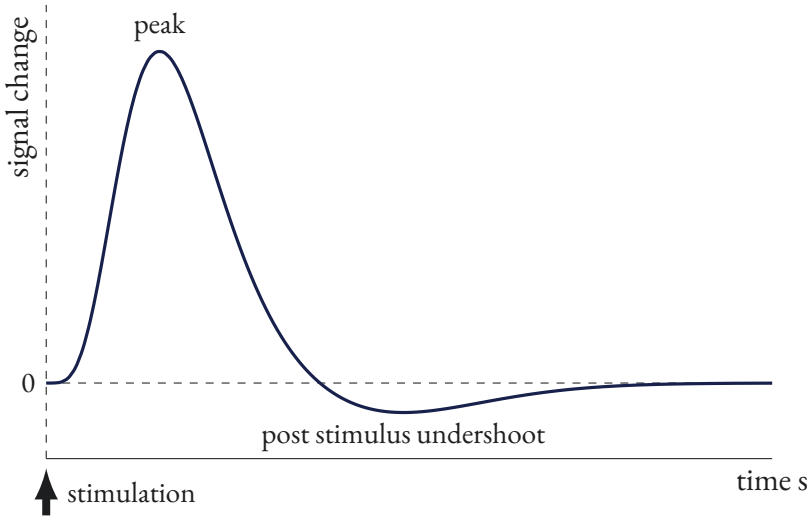

Figure 2.12: Haemodynamic Response Function. After the stimulus the peak appears after around 5 s followed by the signal reduction and a small undershoot. All parameters of the HRF are as well subject-specific as specific for different brain regions.

The increase in blood flow in active areas is delayed by several seconds after the stimulation. After this delay, the BOLD effect reaches its maximum, followed by a decrease and a small undershoot. This time-course is modelled by the so-called Haemodynamic Response Function (HRF) in Figure 2.12. One modelling approach employs the difference of two Gamma distributions

$$HRF(x) = g_1(x, k_1, l_1) - A * g_2(x, k_2, l_2) \tag{2.22a}$$

$$g(x, k, l) = \frac{x^{k-1} e^{-x/l}}{l^k * \Gamma(k)} \tag{2.22b}$$

with shape parameter h and scale parameter l, each dependent on the peak positions and standard deviations of the respective gamma distribution, and an additional scale factor A.

2.5.2 Echo Planar Imaging

In order to obtain activation maps, fMRI data sets are typically fitted to a model representing the expected activation time courses. High temporal resolution is necessary to cover such signal changes. To meet these requirements, functional MRI images are typ-

Die approbierte gedruckte Originalversion dieser Diplomarbeit ist an der TU Wien Bibliothek verfügbar.
The approved original version of this thesis is available in print at TU Wien Bibliothek.
TU Bibliothek Your knowledge hub WIEN

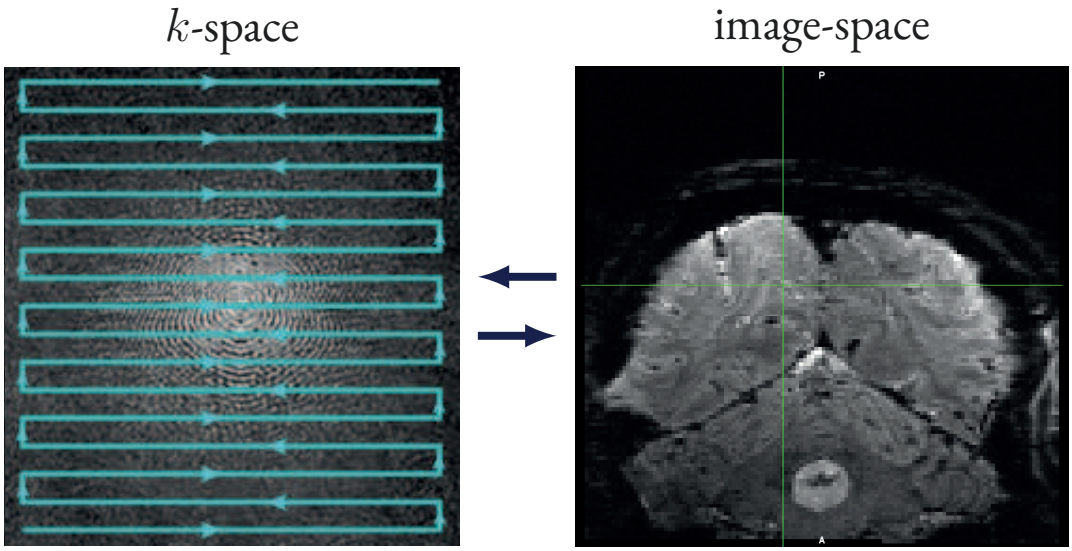

Figure 2.13: Acquisition of a 2D single-shot EPI image in k-space, starting in the bottom left corner and then acquiring line by line. The corresponding gradient sequence is shown in Figure 2.14. On the right-hand side, a typical slice of the occipital lobe is shown. [11]

ically recorded using a particular k-space acquisition method, the so-called echo-planar imaging (EPI). In the single-shot variant of this sequence, all data of one slice is acquired after a single excitation pulse. The gain in temporal resolution, however, goes along with increased noise ratios and other challenges.

During the acquisition of an EPI image, not only one line of the k-space is measured after every excitation as in classical imaging. Through rapid switching of the gradient fields G_x and G_y, the whole k-space of one image slice is sampled after each excitation pulse, as seen in Figure 2.13. One important time constant is the so-called repetition time (TR) which is the time it needs to measure the whole 3D volume once, so in other words, after every TR one time-point is added to every voxel. The sequence diagram is shown in Figure 2.14. The echo time (TE) in EPIs is replaced by an effective echo time, which is defined as the time between the excitation pulse and the time when the central lines of k-space are filled.

Hand in hand with the possibility for high-speed imaging, several challenges may occur. For example, due to small inhomogeneities of the static magnetic field $\vec{B}_0$, caused by different magnetic susceptibilities of tissues inside the scanner. These small magnetic

Die approbierte gedruckte Originalversion dieser Diplomarbeit ist an der TU Wien Bibliothek verfügbar.
The approved original version of this thesis is available in print at TU Wien Bibliothek.
TU Bibliothek Your knowledge hub WIEN

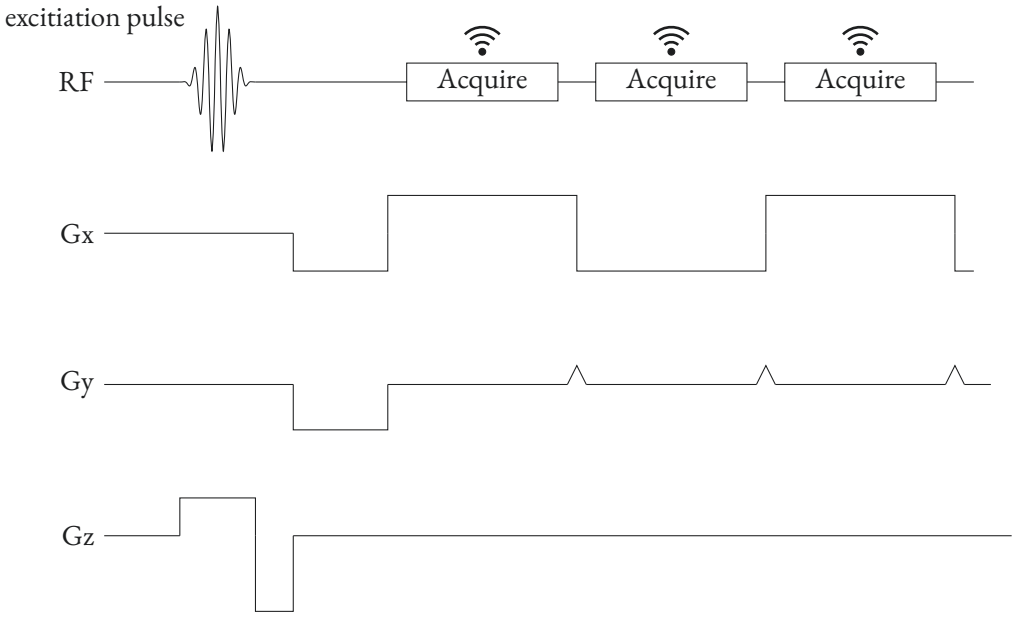

Figure 2.14: Single-shot 2D EPI sequence. Directly after the 90° rf-pulse with the corresponding slice selection gradient G_z, the acquisition is started at the bottom left corner of k-space, as seen in Figure 2.13. Afterwards the gradient G_x moves the acquisition along a horizontal line, while the small blips by the G_y-gradient cause it to jump to the next k-space line.

Die approbierte gedruckte Originalversion dieser Diplomarbeit ist an der TU Wien Bibliothek verfügbar.
The approved original version of this thesis is available in print at TU Wien Bibliothek.

field changes alter the spin rotation frequency very locally, and therefore the voxels are shifted on the resulting image, which may also lead to information from several voxels being compressed into a small area. This effect is called geometric distortion and is highly dependent on the field strength. EPIs are most severely affected by distortion as the whole k-space is sampled after a single excitation pulse and therefore phase errors sum up while moving through k-space in y-direction.

Geometric distortions can be minimized before the scan begins by the so-called shimming procedure where special coils are used to minimize field inhomogeneities. However, this is not sufficient at ultra-high magnetic fields and therefore correction on the acquired data is necessary. Mainly two different methods for the distortion correction are established. With the fieldmap method a B_0 map is measured without excitation [12], which is used to calculate a displacement map for the correction. The second method uses the FSL Topup program [13, 14] where the displacement map is calculated from two EPI images with inverted phase-encoding direction (e.g. LR and RL) by minimizing the sum-of-squares differences between the two images.

In the EPI acquisition scheme, as shown here, the k-space is filled beginning in the bottom left corner and then continuing through it line-by-line. While this is the most often used trajectory for ultra-fast imaging, it is not the only variant for sampling the whole k-space after one excitation. Other k-space trajectories start at the image centre and then spiral out, or sample the space in a star-shape. The choice of the path through the k-space is dependent on the used imaging method and individual needs.

Die approbierte gedruckte Originalversion dieser Diplomarbeit ist an der TU Wien Bibliothek verfügbar.
The approved original version of this thesis is available in print at TU Wien Bibliothek.
TU Bibliothek Your knowledge hub WIEN

3 The Visual System

The following chapter gives a brief introduction into the human visual system since in this work the visual cortex was examined [15].

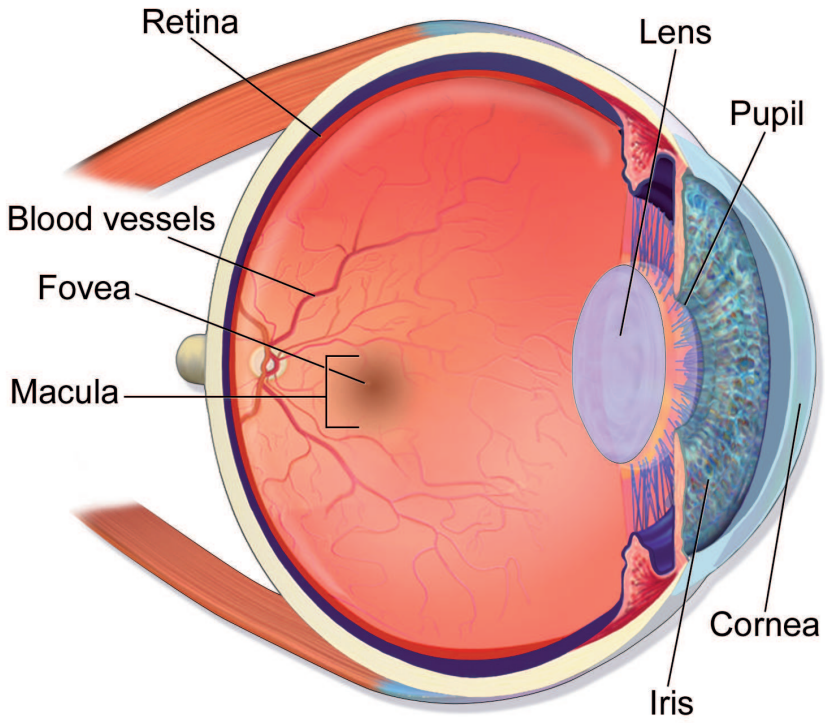

Figure 3.1: Anatomy of the human eye. Light is focused on the retina, where the photoreceptors are located, by the cornea and the lens and have to pass the iris and the pupil. The macula and in special the fovea represent the central visual field. The signal moves further to the optical disk and nerve, located where the blood vessels meet. [16]

Die approbierte gedruckte Originalversion dieser Diplomarbeit ist an der TU Wien Bibliothek verfügbar.
The approved original version of this thesis is available in print at TU Wien Bibliothek.
TU Bibliothek Your knowledge hub WIEN

3.1 Retina

The first subpart of the human visual system is the retina. After focusing by the cornea and the lens, the light passes through the vitreous humour to fall on the retina. There the light is absorbed by the photoreceptors. The hundreds of millions of cells can morphologically be divided into two types, the rod and the cone cells.

Functionally these two cell types differ. In low-light condition, the rod cells can build the highly light-sensitive protein rhodopsin which enables for vision in dark conditions, but again splits up under stronger illumination. Vision under better light conditions is mainly enabled by the cone cells. Their specific photoreceptive protein is photopsin, which is stable under strong illumination. The rod cells can be again divided into three subcategories, sensitive for different wavelengths, and therefore responsible for colour vision.

Interestingly, the distribution of rod and cone cells is not evenly throughout the retina (Figure 3.2). The number of cones is peaking in the macula lutea with their highest density in the fovea. This enables for very high-contrast vision right in the centre of the visual field. While the density of cones is very low outside the macula, the number of rods has the opposite distribution. While there are almost no rods in the macula, the peak of rod-density is around 20° visual angle from the fovea.

The stimulation of photoreceptor cells is transmitted towards the optic nerve head, also called the optic disk. At this part of the retina, not photoreceptor cells are located, which leads to a blind spot. The information is further transported for about 50 mm until both eyes optic nerves meet at the chiasma. At this point, the optic nerves reorganize. Nasal nerve fibres cross sides while temporal fibres stay on their side. This results in a new organization where the left hemifield of view is transferred to the right hemisphere and vice versa. Also, this means that information from both eyes is transferred to either hemisphere. The path of the optic nerve is shown in Figure 3.3.

Die approbierte gedruckte Originalversion dieser Diplomarbeit ist an der TU Wien Bibliothek verfügbar.
The approved original version of this thesis is available in print at TU Wien Bibliothek.
TU Bibliothek Your knowledge hub WIEN

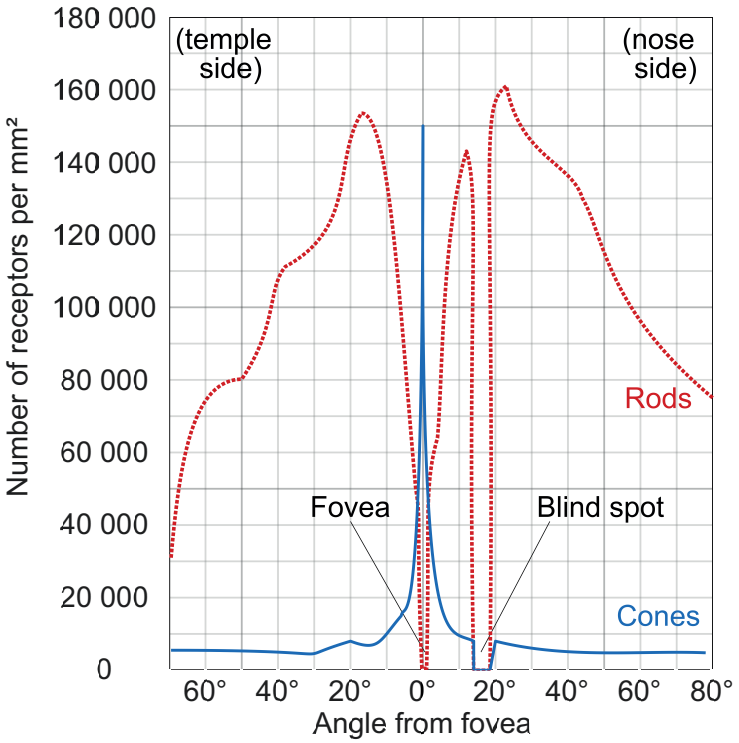

Figure 3.2: Distribution of rods and cones on the retina. Most cones are present on the macula with their peak at the fovea, while cones are less represented in me macula and peak at around 20° visual field angle. At the optic disk, where the visual nerve enters, no rods and cones are located. [17]

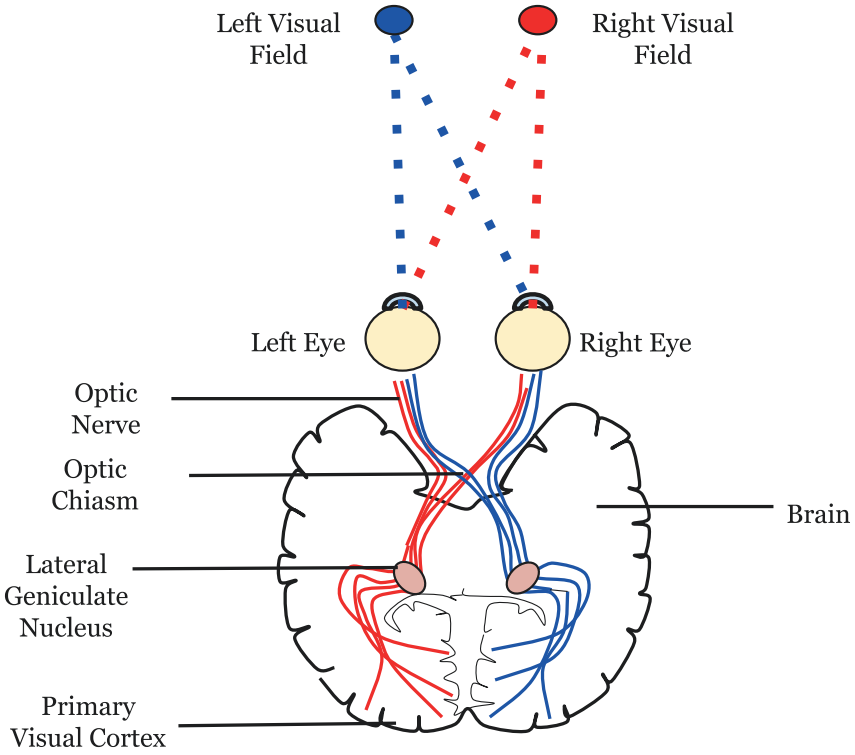

Figure 3.3: The neural pathway of the optic nerve. Beginning at the optic never heads in each eye the optic nerves meet at the chiasma, where it is rearranged based on the corresponding visual field position. Information from the left hemifield is transferred to the right optic tract and vice versa. [18]

Die approbierte gedruckte Originalversion dieser Diplomarbeit ist an der TU Wien Bibliothek verfügbar.
The approved original version of this thesis is available in print at TU Wien Bibliothek.
TU Bibliothek Your knowledge hub WIEN

3.2 Visual Cortex

Originating from the chiasma, the visual nerve splits up to several areas associated with the visual system, amongst others, areas responsible for eye movement or the pupillary light reflex. Most fibres lead to an ipsilateral relay nucleus, the so-called lateral geniculate nucleus (LGN) (Figure 3.3) from where they lead to the primary visual cortex (V1) in the occipital lobe of the respective hemisphere. The exact location of V1 is around the calcarine sulcus on the medial side of the occipital lobe. The signal is further distributed to more than 20 higher areas including V2, V3, V4 and V5. Each area has unique functional specialisations. The visual system is not strictly bottom-up organized, which means that higher areas can feedback to earlier areas (top-down).

The further processing of information from the visual system can be roughly divided into two streams (Figure 3.4), the ventral ("What") and dorsal ("Where") [19]. While the ventral stream processes information regarding the recognition of faces and objects, the dorsal stream leads to brain regions responsible for spatial orientation and localisation of objects.

The fact that the topological representation of the retina is preserved through the whole visual system up to the visual cortex enables for the method of retinotopy. There a definite, subject-specific mapping between the retina, respectively the visual field, and the position on the cortex is obtained.

Die approbierte gedruckte Originalversion dieser Diplomarbeit ist an der TU Wien Bibliothek verfügbar.
The approved original version of this thesis is available in print at TU Wien Bibliothek.
TU Bibliothek Your knowledge hub WIEN

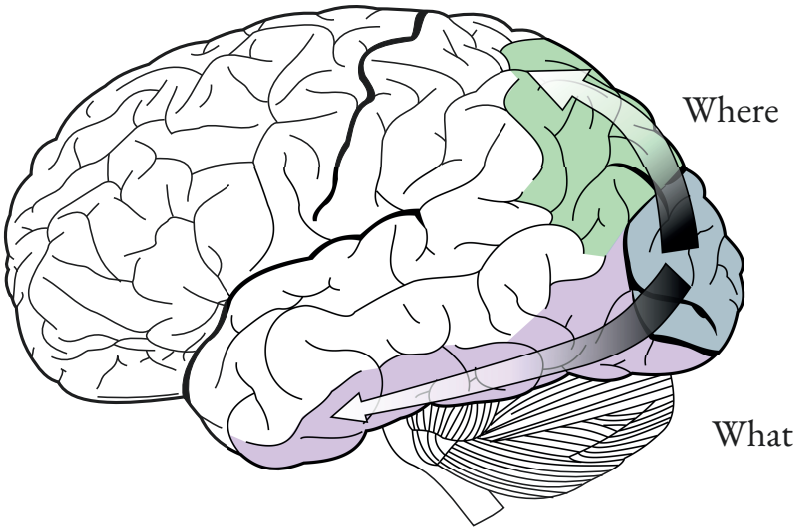

Figure 3.4: Two main pathways lead from the visual system (blue). The dorsal ("Where") stream is responsible for orientation while the ventral ("What") stream processes the recognition of objects. [20]

Die approbierte gedruckte Originalversion dieser Diplomarbeit ist an der TU Wien Bibliothek verfügbar.
The approved original version of this thesis is available in print at TU Wien Bibliothek.
TU Bibliothek Your knowledge hub WIEN

4 Retinotopic mapping

First retinotopic maps have been created after World War I when primarily Japanese and British doctors noticed correlations between visual field losses and areas of the primary visual cortex, wounded by gunshots [21, 22]. In the late 20th-century, fMRI was introduced and emerged as a perfect tool for the creation of retinotopic maps. Engel [1] was the first to present flickering expanding rings to centrally fixating subjects inside an MRI scanner and therefore stimulating areas of the visual cortex periodically. The BOLD activation on the visual cortex was therefore represented as a travelling wave, where the phase encodes visual field eccentricity (Figure 4.1). The phase-shift of every spatial position along the region of interest (ROI) can be calculated by applying a 1D Fourier transformation and is respectively linked to an eccentricity value.

Another, more recent approach for retinotopic mapping is called population Receptive Field (pRF) mapping and was introduced by S. O. Dumoulin and B. A. Wandell in 2008 [2]. The method is described in more detail in the next chapter. In short, the receptive field of every voxel is estimated with a specific model, typically a two-dimensional Gaussian with fitting parameters x and y for position and σ for the standard deviation. For every voxel, these pRF model parameters are optimised in order to fit the voxel's recorded time series as close as possible.

Die approbierte gedruckte Originalversion dieser Diplomarbeit ist an der TU Wien Bibliothek verfügbar.
The approved original version of this thesis is available in print at TU Wien Bibliothek.
TU Bibliothek Your knowledge hub WIEN

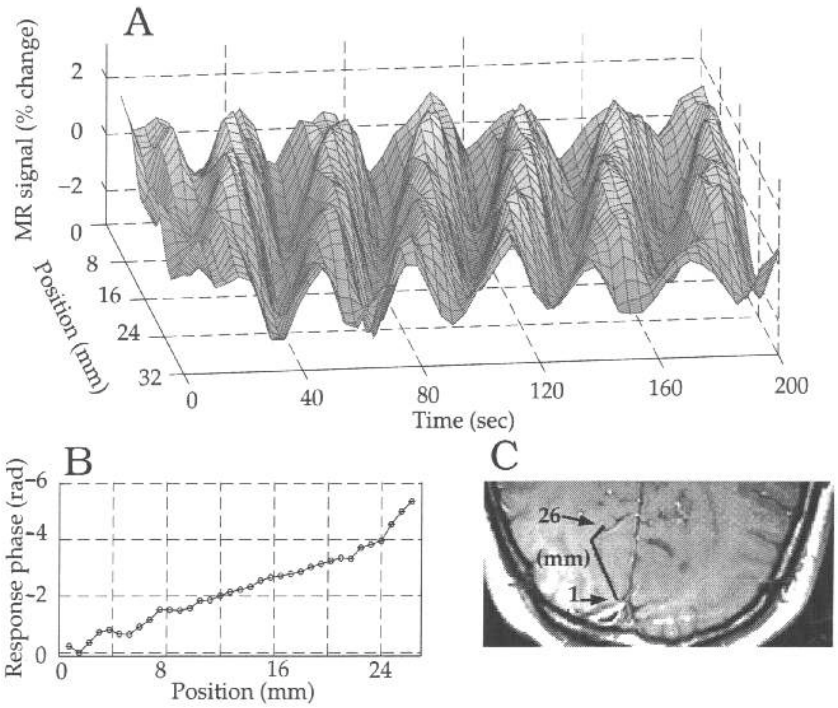

Figure 4.1: In A the travelling wave of the fMRI signal over the ROI and time, observed in the primary visual cortex (V1) is shown. The stimulus consisted of 6 blocks of expanding ring; each block lasted 32 s. B shows the phase in radians over the spatial position along the ROI at one time-point. C defines the ROI along the calcarine sulcus on an anatomical image. [1]

4.1 Visual Stimuli

Since it is not necessary to use periodical stimuli with the pRF analysis, there are lots of different possibilities in order to design the retinotopic stimulus. However, not every stimulus is suitable for retinotopy since there are several aspects which have to be considered. As an example, completely random appearing segments of stimulus rings [23] could achieve the maximum difference in the recorded voxel time courses, which should also lead to better model fits. These random stimuli, however, tempt the subject to lose the fixation on the central spot and subconsciously saccade towards the appearing stimuli. Furthermore, for different areas of interest on the visual field of view and on the visual cortex, appropriate stimuli can be chosen.

The most commonly used stimulus shapes include Dumoulin's travelling bar stimulus and Engel's rotating wedges and expanding ring stimulus, both shown in Figure 4.2.

Die approbierte gedruckte Originalversion dieser Diplomarbeit ist an der TU Wien Bibliothek verfügbar.
The approved original version of this thesis is available in print at TU Wien Bibliothek.
TU Bibliothek Your knowledge hub WIEN

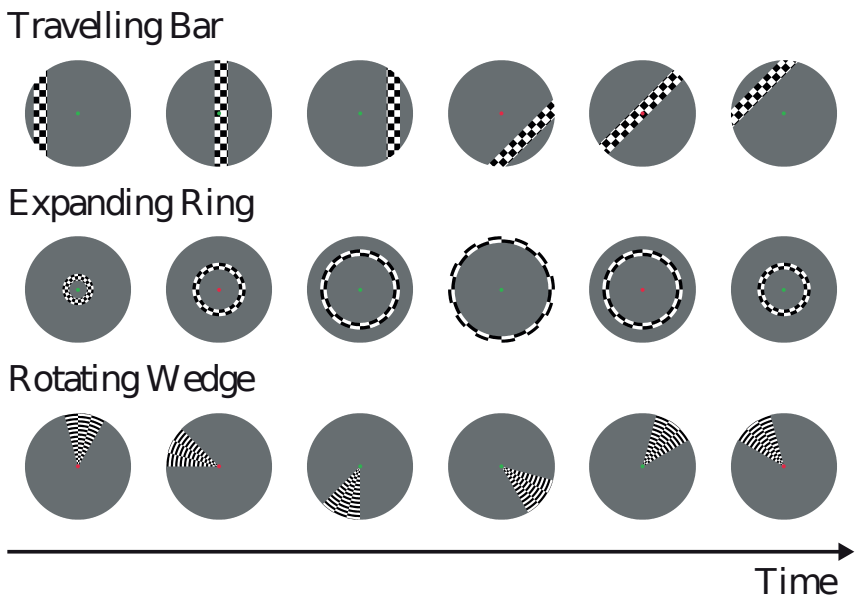

Figure 4.2: Commonly used retinotopic mapping stimuli. While the travelling bar stimulus can be used for the pRF analysis by itself, the rotating wedge and expanding ring stimuli have to be combined to allow the estimation of the complete positional information [25].

Here, the stimulus shapes are filled with a flickering checkerboard (8 Hz); other variants use rapidly presented natural pictures instead [24].

In our implementation, the travelling bar stimulus is built up of eight blocks, each built up from a bar of a certain thickness, which crosses the field of view from eight different directions with a discrete number step size, starting from left to right and afterwards rotating clockwise by 45° following every passing. After every second crossing, a short pause is inserted.

On the other hand, the wedges and rings stimulus consists of four blocks. The first and third block contains the rotating wedge which travels two full rounds in opposite directions. The second and fourth block show the ring, first expanding from the centre to the edges and then contracting back to the centre. While the second block starts at the centre, the fourth block begins at the edges of the field of view, in order to maximize voxel time-course differences.

We use the basic implementation of both stimuli, which can be customised in various forms. The simplest change of stimulus parameters is the adaption of the stimulus width, either to a fixed value or dependent on another parameter such as eccentricity. An eccen-

Die approbierte gedruckte Originalversion dieser Diplomarbeit ist an der TU Wien Bibliothek verfügbar.
The approved original version of this thesis is available in print at TU Wien Bibliothek.
TU Bibliothek Your knowledge hub WIEN

tricity dependent bar stimulus would have the advantage of covering the central parts of the visual field more accurately [26].

4.2 fMRI Measurement

The setup for an fMRI experiment includes a stimulus presentation system suitable for the used scanner. This can either be an LED screen placed at the end of the bore or a projector, and a rear projection screen fixed at the back end of the patient table. Further, a small mirror is placed inside the head coil, through which the subject can see the screen. Stable fixation is particularly important for retinotopy, and therefore a fixation dot is presented in the screen centre. In most implementations, the dot changes colour at irregular intervals, and the subject is asked to report colour changes by pressing a button in order to measure fixation performance.

For retinotopic mapping, brain coverage is limited to a small number of slices which are located on the occipital lobe, perpendicular to the calcarine sulcus. This limitation is important, since higher resolutions are possible on smaller areas, and high-quality images are needed. Since wraps, caused only in phase encoding direction, from other parts of the brain would corrupt the images, the phase encoding direction is chosen left-right.

Additionally, a T_1 weighted whole-brain image is acquired, as well as additional scans for the distortion correction [27, 28].

4.3 Pre-Processing

After the measurement, fMRI data are not immediately suitable for analysis. This is because BOLD-related signal changes in fMRI are only in the order of a few percent, and data sets are typically affected by artefacts from numerous non-neural sources. Thus, several pre-processing steps have to be performed in order to correct the data for these artefacts. In our case, those steps are mainly performed using Freesurfer (Martinos Center for Biomedical Imaging, Charlestown, Massachusetts), and the Matlab (The MathWorks Inc., Natick, Massachusetts) based SPM toolbox (Welcome Trust Centre for Neuroimaging, London, UK).

Die approbierte gedruckte Originalversion dieser Diplomarbeit ist an der TU Wien Bibliothek verfügbar.
The approved original version of this thesis is available in print at TU Wien Bibliothek.
TU Bibliothek Your knowledge hub WIEN

Slice-time correction The EPI sequence used, acquires one 2D slice after another and subsequently combines the slices to a 3D volume. As not all slices can be acquired simultaneously, it is necessary to temporarily shift the slices towards a reference slice.

Realignment Due to small movements of the subject, not every 3D volume is aligned perfectly throughout a scanning session. The realignment step corrects for these small spatial displacements.

Distortion correction Especially at ultra-high fields, small inhomogeneities in the static magnetic field $\mathbf{B_0}$ lead to geometrical distortions in EPI images. Additional to the shimming process performed at the scanner, distortion correction is needed in during pre-processing. The most common correction methods are based on either directly recording the inhomogeneities using a fieldmap or recording images distorted in opposing directions. After the calculation of displacement maps, the distortion correction is applied to the functional runs.

Smoothing To further remove the effects of small movements, spatial smoothing, using a Gaussian kernel can be used.

Segmentation The segmentation into grey and white matter is performed automatically on the anatomical T_1-weighted image by Freesurfer's '*recon-all*' pipeline. Afterwards, the grey matter mask is manually corrected for potential segmentation errors using the tool ITKGray (`https://web.stanford.edu/group/vista/cgibin/wiki/index.php/ItkGray`).

4.4 pRF Analysis

For the pRF model fitting, the MATLAB toolbox mrVista (`https://web.stanford.edu/group/vista/CGI-bin/wiki/index.php/MrVista`) is used. The fitting procedure requires the anatomical image, the functional runs and a so-called inplane anatomy image (anatomical image with the same dimension and orientation as the functional images), all shown in Figure 4.3. Further, the stimulus images and parameters as given input (4.2). Additionally, the white matter mask is passed to mrVista, which grows three layers of grey matter

Die approbierte gedruckte Originalversion dieser Diplomarbeit ist an der TU Wien Bibliothek verfügbar.
The approved original version of this thesis is available in print at TU Wien Bibliothek.
TU Bibliothek Your knowledge hub WIEN

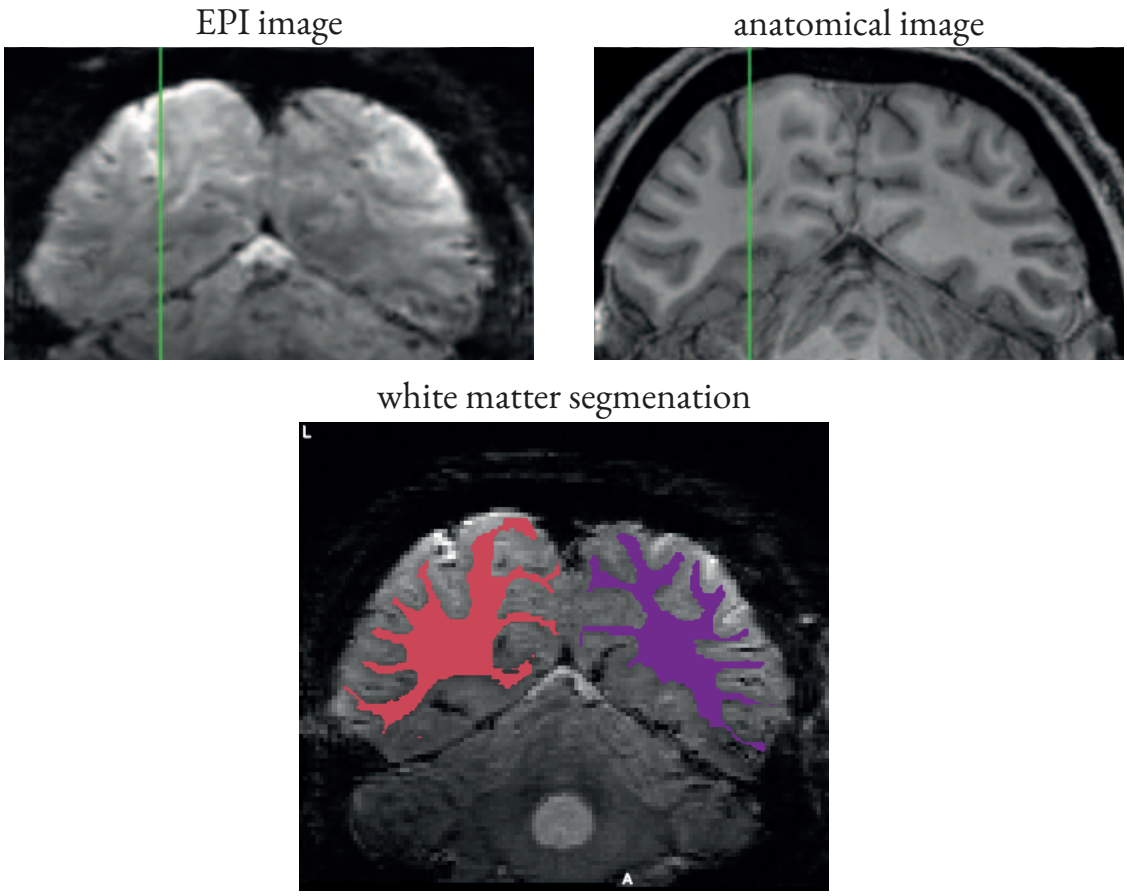

Figure 4.3: An the top, one slice of the functional EPI image of the occipital lobe is shown with its corresponding inplane anatomy image. At the bottom, the coloured white matter mask is shown on top of an anatomical image.

on top. This grey matter mask determines the voxels which time-courses are used for the fitting procedure.

The fitting procedure is built up of several stages, from coarse-to-fine. The result of a previous step is always prior for the next optimisation step. For every point on the visual field, mrVista calculates model time courses, with the parameters x and y as position on the visual field and σ as the FWHM of the model-specific Gaussian. The time-courses based on the stimulus are discrete, 0 if there was no stimulus and 1 if there was one. These war time-courses have to be folded with the HRF in order to later fit to the voxels time-courses. Starting from initial values of x, y and σ for every voxel in the grey matter mask,

Die approbierte gedruckte Originalversion dieser Diplomarbeit ist an der TU Wien Bibliothek verfügbar.
The approved original version of this thesis is available in print at TU Wien Bibliothek.
TU Bibliothek Your knowledge hub WIEN

the residual sum of squares (RSS), between the measured and the model time course, is minimized by changing the parameters. This is calculated as follows:

$$RSS = \sum_t (y(t) - p(t)\beta_1 - \beta_2)^2 \tag{4.1}$$

where $y(t)$ represents the data and $p(t)$ the predicted model. The β parameters account for amplitude β_1 and offset β_2 of the MRI signal. Additionally, subject-specific differences in the haemodynamic delay are compensated by a fitting-stage, where the HRF is optimized. The fitting procedure flow chart is shown in Figure 4.4.

After this process is repeated for every grey matter voxel, the output is a parameter map which contains the position and size of the population receptive fields linked to all grey matter voxels. The result can be visualized in different ways, as seen in Figure 4.5 and Figure 4.6.

One parameter for comparing the performance of the fitting process is the relative variance explained by the pRF model in the recorded time series. This parameter can be used as a threshold in order to visualize voxels, where the model fit is satisfactory.

The essential parameters of every pRF, beside variance explained, are eccentricity, polar angle and pRF size. These parameters encode the position (eccentricity as radius and polar angle) on the visual field as well as the size of the pRF for every voxel.

The human visual system is built up from several complex parts, starting at the eye, the optic nerve and the brains visual system. Latter is again partitioned in several functional areas which are distributed in a specific order and responsible for different parts of the visual signal processing. The lowest subsystem is the so-called primary visual cortex (V1), located around and in the calcarine sulcus on the occipital lobe. V1 can be easily segmented using functional MRI data, see Figure 4.7. The segmentation follows the borders of visual field regions V1 and V2, which are characterized by phase reversals of the polar angle parameter. In the visual field, these borders correspond to the vertical meridian.

Die approbierte gedruckte Originalversion dieser Diplomarbeit ist an der TU Wien Bibliothek verfügbar.
The approved original version of this thesis is available in print at TU Wien Bibliothek.
TU Bibliothek Your knowledge hub WIEN

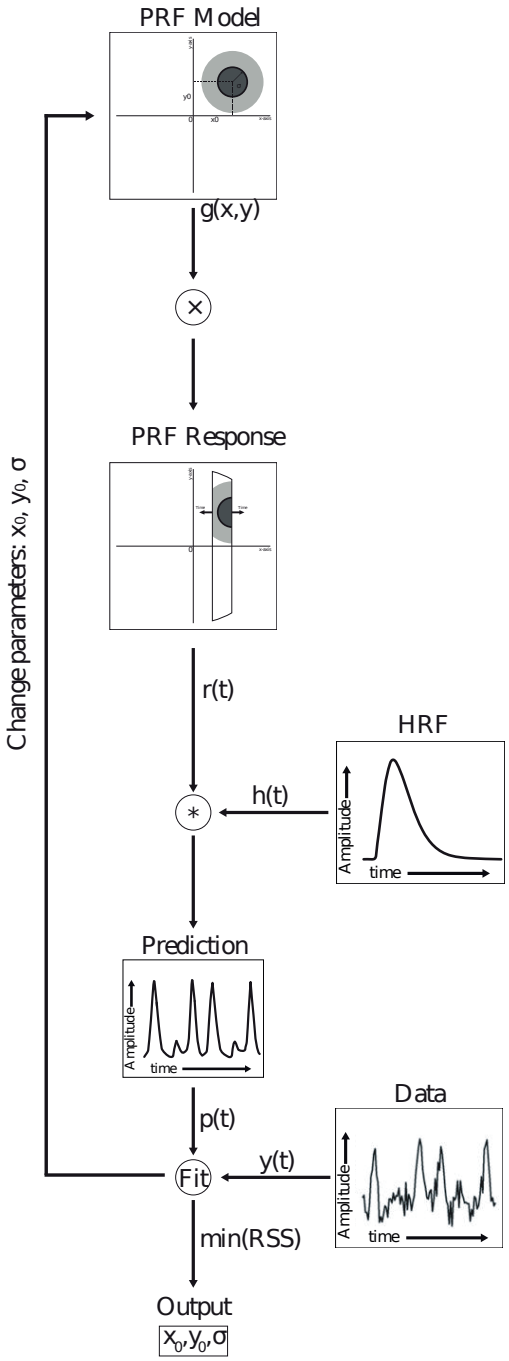

Figure 4.4: Fitting process in mrVista. The parameters position (x_0, y_0) and size (σ) of the pRF for every voxel are modified until the residual sum of squares (RSS) between the current model estimation and the recorded time series is minimal [2]

Die approbierte gedruckte Originalversion dieser Diplomarbeit ist an der TU Wien Bibliothek verfügbar.
The approved original version of this thesis is available in print at TU Wien Bibliothek.

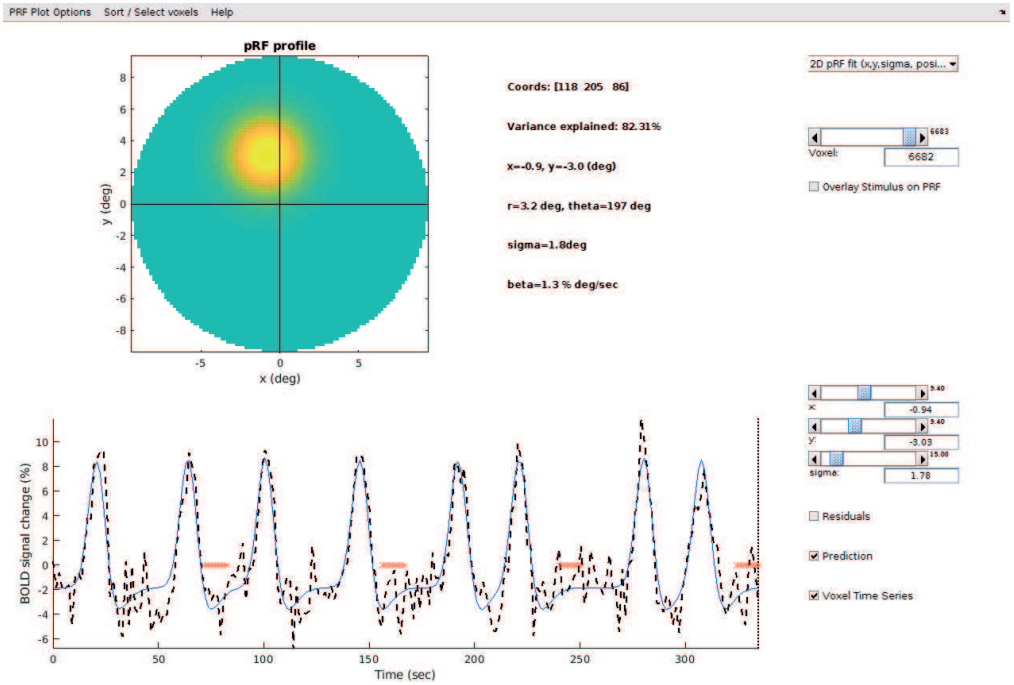

Figure 4.5: The pRF model for a single voxel. On the bottom the measured time series (black) and the estimated model (blue) is shown. On the top left the total stimulated visual field and the estimated pRF for this voxel (yellow) is illustrated.

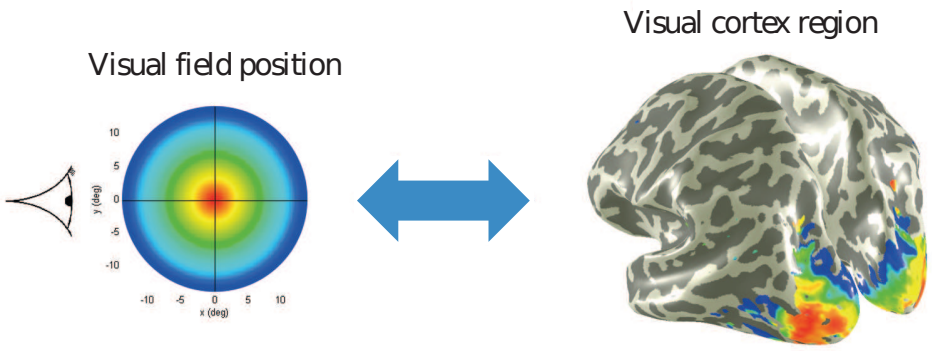

Figure 4.6: Retinotopic eccentricity map on an inflated 3D WM/GM mesh on the right side. The colours are coded as seen on the left-hand side, where the central positions are red, and the peripheral areas are in blue. As known from the literature, the central position on the visual field is mapped to the occipital pole while more peripheral regions correspond to more anterior regions on the cortex.

Die approbierte gedruckte Originalversion dieser Diplomarbeit ist an der TU Wien Bibliothek verfügbar.
The approved original version of this thesis is available in print at TU Wien Bibliothek.
TU Bibliothek Your knowledge hub WIEN

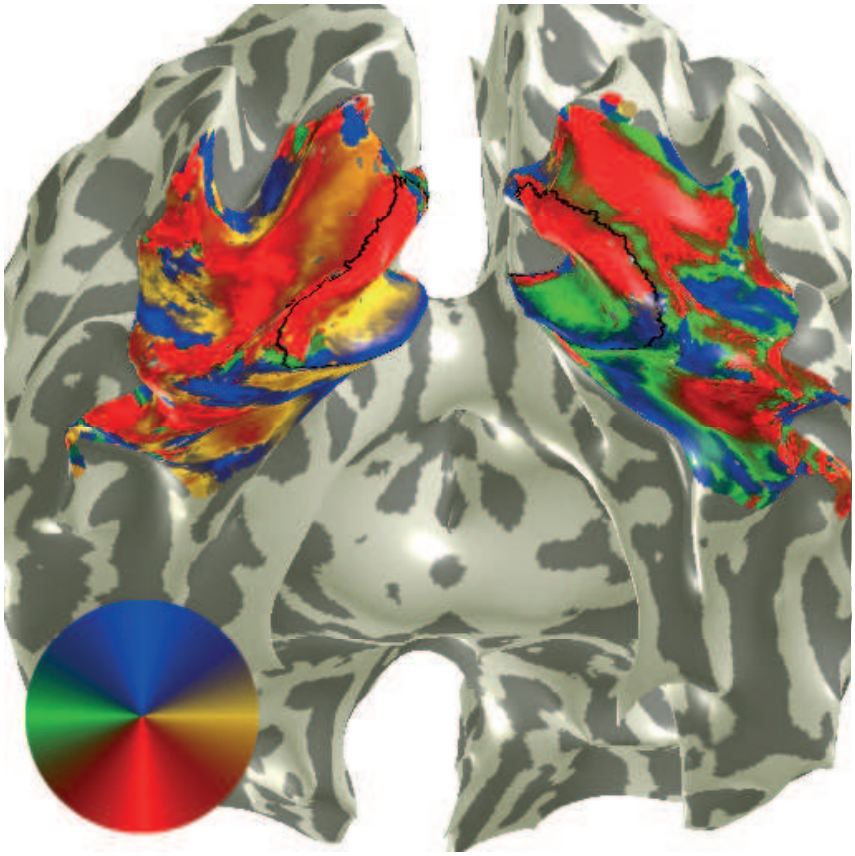

Figure 4.7: Retinotopic polar angle map with V1 segmentation (black line) and no variance explained threshold. The colour coding of subject's visual field is seen in the bottom left corner.

Die approbierte gedruckte Originalversion dieser Diplomarbeit ist an der TU Wien Bibliothek verfügbar.
The approved original version of this thesis is available in print at TU Wien Bibliothek.
TU Bibliothek Your knowledge hub WIEN

5 Improved population receptive field mapping by combining stimulus subtypes

5.1 Overview

fMRI allows for the in-vivo investigation of activity, among other regions, in the visual cortex. The method, mapping the visual field onto the cortex is called retinotopy, and in special experiments are carried out using the population receptive field (pRF) method. In these experiments, sequences of visual stimulation by flickering checkerboard shapes are used to cause related BOLD responses on certain visual cortex positions. Two stimulus variants are common, the travelling bar and the wedges and rings stimulus. The choice of the stimulus variant is heavily affecting the analysis result. These two variants are compared in healthy subjects, and a novel combination method is introduced, in order to combine both stimuli's specific strengths.

5.2 Introduction

Retinotopy refers to the preservation of retinal adjacency via the visual stream to the primary visual cortex. It is one of the most remarkable features in human visual neuroanatomy. Among the first reports on topographical (retinotopic) maps were lesion studies in soldiers that showed correlations between visual field positions and visual cortex regions [21, 22, 29].

Magnetic resonance imaging enabled for further investigation of the visual system. Anatomical imaging, in combination with lesion studies, enabled for the observation of

Die approbierte gedruckte Originalversion dieser Diplomarbeit ist an der TU Wien Bibliothek verfügbar.
The approved original version of this thesis is available in print at TU Wien Bibliothek.
TU Bibliothek Your knowledge hub WIEN

cortical magnification factors [30] as well as cortical thickness measurements [31]. Functional magnetic resonance imaging (fMRI) is ideally suited for studying retinotopy as shown in the seminal studies by Engl and others [1] (for a review see, e.g. [32]). They used a travelling wave paradigm where concentric, expanding rings were presented to the participants. These flickering checkerboard stimuli were designed to maximise the BOLD effect on the visual cortex. The expanding rings appeared periodically on the visual field and thus caused sinusoidal activation time-curses in the visual cortex where the phase encodes the position in the visual field.

Population receptive field (pRF) mapping represents an extension of the earlier retinotopic mapping approaches as it allows for a more detailed characterisation of the representation of the visual field on the cortical surface [2]. Here, a receptive field (RF) describes the representation of a specific visual cortex area on the visual field and therefore on the retina. Due to limited spatial resolution, it is not possible to investigate single neuron activities, which means that every voxel in the fMRI data-set represents a considerable population of neurons. In the most straightforward case, the fitting process estimates each voxel's pRF as a two-dimensional Gaussian function with the parameters position (x, y) and size (σ). Modified fitting functions such as a difference of Gaussians [33] or an elliptical Gaussian [34] were also suggested. The parameters are optimised for each voxel so that the associated model time course optimally fits the recorded fMRI data.

Various visual stimuli can be used for pRF mapping. Modifying the original Engel stimulus consisting of expanding rings, which only encodes for eccentricity, Sereno and colleagues [35] proposed rotating wedges to estimate the polar angle parameter and therefore the absolute pRF position shortly after. Dumoulin and Wandell introduced another commonly used stimulus which uses flickering bars moving through the field of view in different directions. Other papers introduced new or slightly modified stimulus variations to improve accuracy compared to conventional monochrome checkerboards, e.g. visual stimuli involving natural scenes [36, 37] and chromatic stimuli [38]. Also, stimulus shapes were modified in order to improve mapping results [26, 39].

Nevertheless, expanding ring/rotating wedge and bar stimuli are the most often used variants in pRF mapping today. They are primarily used for historical reasons rather than based on extensive modelling. While both stimuli are known to achieve good results, both have, however, their specific strengths and weaknesses which can be seen in pRF mapping results [25]. In this study, we aimed at comparing pRF mapping results of these

Die approbierte gedruckte Originalversion dieser Diplomarbeit ist an der TU Wien Bibliothek verfügbar.
The approved original version of this thesis is available in print at TU Wien Bibliothek.
TU Bibliothek Your knowledge hub WIEN

two stimulus variants using fMRI at the ultra-high magnetic field (7T). Also, we aimed at combining both approaches to overcome the variant-specific shortcomings.

5.3 Methods

5.3.1 Subjects

Ten subjects (6 male, 4 female; age 25.1±3) participated in the experiment. Subjects had normal visual acuity and no history of significant eye disease. Subjects were naive to the experiment and were introduced to the stimuli only shortly before the measurement; they received no further training. Subjects gave informed consent and received financial compensation for their participation. The local ethics committee approved the study.

5.3.2 MRI measurements

All measurements were performed on a 7T Siemens MAGNETOM scanner using a 32-channel head coil. Functional data were acquired using the CMRR EPI sequence [40] measuring 32 slices with 1 mm isotropic resolution and the following parameters: TE=25 ms; TR=1000 ms; multiband factor=2; GRAPPA acceleration=2; slice spacing=10 %. 336 volumes were acquired per run, corresponding to a run time of about 5.5 minutes. Slices were positioned orthogonally to the calcarine sulcus, covering 35.2 mm of the occipital cortex. Additionally, B_0 field maps were acquired for distortion correction.

Anatomical imaging was performed using a magnetization-prepared rapid gradient-echo (MPRAGE) sequence with 0.7 mm isotropic resolution (TE=3.66 ms; TR=1960 ms).

5.3.3 Stimuli

Two different stimulus variants were used. Each covered the central 14° of the subjects' visual field. Subjects were instructed to fixate on a central dot and to report colour changes of the fixation dot in order to ensure fixation and quantify the subjects' attention during the task. All stimuli are shapes exposing a 8 Hz black-white flickering checkerboard on a grey background.

The first stimulus is derived from the classic "wedge and ring" stimulus. It starts with a counter-clockwise rotating wedge, with a width of 45° and a step size of 10°, performing

Die approbierte gedruckte Originalversion dieser Diplomarbeit ist an der TU Wien Bibliothek verfügbar.
The approved original version of this thesis is available in print at TU Wien Bibliothek.
TU Bibliothek Your knowledge hub WIEN

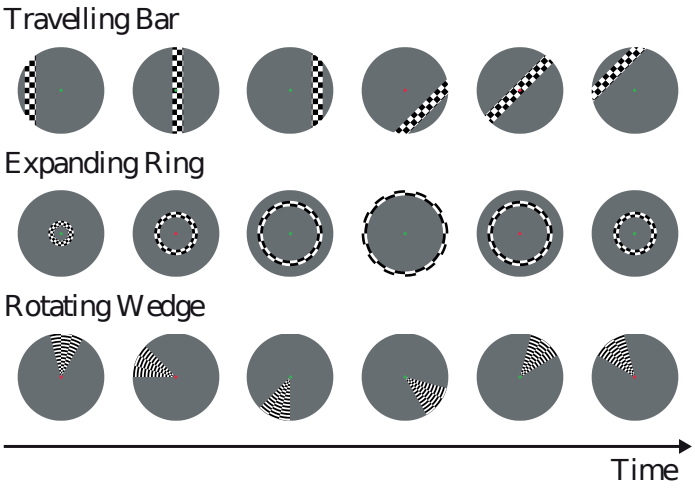

Figure 5.1: While the travelling bar stimulus in the first row can be used by itself to perform pRF analyses, the rotating wedge and expanding ring stimuli have to be combined in order to estimate the unique position. [25]

two full rotations in 72 steps. The second part of the stimulus consists of a ring with a thickness of 2° visual angle and expands from the centre to the edges twice in 72 steps. This whole sequence is repeated a second time, albeit with a clockwise rotating wedge and a contracting ring. Between each wedge and ring period, the grey background was shown for twelve seconds as a baseline.

The second stimulus variant is based on the travelling bars stimulus introduced by Dumoulin and Wandell [2]. The bar starts moving from left to right, with a width of 3° visual angle and a step size of 0.8° visual angle for a total of 36 steps per direction. After every crossing, the bar is rotated by 45° clockwise and crosses the screen again from this direction, for a total of eight different directions. The grey background was shown for twelve seconds after each diagonal crossing as a baseline. Both stimuli are shown in Figure 5.1.

Both stimuli have a total length of 336 s each and were presented two times, for a total of four runs per subject.

5.3.4 Analysis

Functional data preprocessing included slice-timing correction using SPM12 in Matlab 9.6, as well as realignment (SPM) and distortion correction using the acquired field maps and FSL FUGUE. For spatial smoothing, a small Gaussian kernel with 2 mm FWHM

Die approbierte gedruckte Originalversion dieser Diplomarbeit ist an der TU Wien Bibliothek verfügbar.
The approved original version of this thesis is available in print at TU Wien Bibliothek.
TU Bibliothek Your knowledge hub WIEN

is applied. In order to obtain cortical grey matter mask that is required to determine the voxels to be analysed, the Freesurfer image analysis suite (https://surfer.nmr.mgh.harvard.edu) was used to segment the high-resolution MPRAGE anatomical image. Subsequently, grey matter masks were manually corrected for segmentation and topological errors.

For the pRF analysis, as well as stimulus creation, the Matlab toolbox mrVista (https://web.stanford.edu/group/vista/CGI-bin/wiki/index.php/MrVista) was used. The first step in the analysis is the creation of pRF models for every point on the visual field. This is done by creating time courses, which are one when the stimulus is present at a specific position and zero otherwise. Additionally, these block functions are convolved with the specific estimated haemodynamic response function of the subject. Secondly, every voxel in the grown grey-matter mask is modelled as a two-dimensional Gaussian function on the visual field with the parameters x, y and σ. Now, for every voxel, optimisation of the residual sum of squares obtains the optimal parameter set.

$$RSS = \sum_t (y(t) - p(t)\beta_1 - \beta_2)^2 \tag{5.1}$$

with the data $y(t)$, the predicted model $p(t)$ and slope β_1 as well as the intercept β_2.

Subsequent to the pRF analysis, primary visual cortex (V1) was segmented manually based on the functional data (polar angle maps) for every subject.

5.3.5 pRF coverage plot

For the visualisation of the pRF fitting result, a visual field coverage map was calculated for every subject. For this purpose, two-dimensional Gaussian functions were centred on every estimated pRF position. The Gaussians have a height of 1 at their centre, and their standard deviation is equivalent to the fitted pRF size parameter σ from the analysis. For every pixel on the visual field map, the maximum profile of overlapping Gaussians was taken to form the coverage map. As a result, a two-dimensional map, with values between 0 and 1, representing the subjects' visual field was plotted.

In order to ensure, that observed phenomena are stimulus-specific rather than subject-specific, mean coverage maps were created by averaging the single-subject coverage maps across all subjects.

Die approbierte gedruckte Originalversion dieser Diplomarbeit ist an der TU Wien Bibliothek verfügbar.
The approved original version of this thesis is available in print at TU Wien Bibliothek.
TU Bibliothek Your knowledge hub WIEN

5.3.6 Combination strategies of pRF runs

Different methods for combining the four available runs per subject (two "wedge and ring", two "travelling bar") were tested.

The first type of combination was the concatenation of the two "eight-bar" and the two "wedge and ring" runs, respectively, prior to pRF analysis. This leads to runs of twice the length and therefore twice as many data points for higher fit accuracy. These fits were used to compare the two different stimuli types.

To achieve a more sophisticated coverage map, a novel combination method is introduced. The original analyses are combined by choosing the model with the highest variance explained in every single voxel. The combination was applied with different underlying analyses. The combination is based on two different sets of pRF analyses:

A the two results of concatenated "eight-bar" and concatenated "wedge and ring" runs.

B all four single run analyses, consisting of to separate "eight-bar" and separate "wedge and ring" runs.

5.4 Results

For all subjects, pRF analyses yielded the expected patterns of eccentricity, polar angle and pRF sizes. Since subjects were all young and had normal visual acuity, we expected uniform coverage maps. Figure 5.2 shows coverage maps resulting from "wedges and rings" and "travelling bar" stimulus runs of a typical subject. Both stimuli exhibit strengths and weaknesses regarding their influence on pRF model estimation as their visual field coverage maps differ in various aspects. While the coverage map based on "wedges and rings" shown in Figure 5.2A has a higher density of pRF in the centre of the visual field, the "travelling bar" stimulus in Figure 5.2B leads to higher pRF coverage in peripheral regions and therefore a more uniform coverage of the visual field.

Similar patterns can be seen when showing the parameter maps overlaid on the visual cortex in Figure 5.3, where results of the two stimulus types are shown in the first two columns. Each row represents a different parameter of the pRF analysis. As in all plots, only voxels with higher than 10 % variance explained are shown. It can be seen that all retinotopic parameters yield the expected shapes, irrespective of the stimulus and combination method used: eccentricity maps show that central parts of the visual field are

Die approbierte gedruckte Originalversion dieser Diplomarbeit ist an der TU Wien Bibliothek verfügbar.
The approved original version of this thesis is available in print at TU Wien Bibliothek.
TU Bibliothek Your knowledge hub WIEN

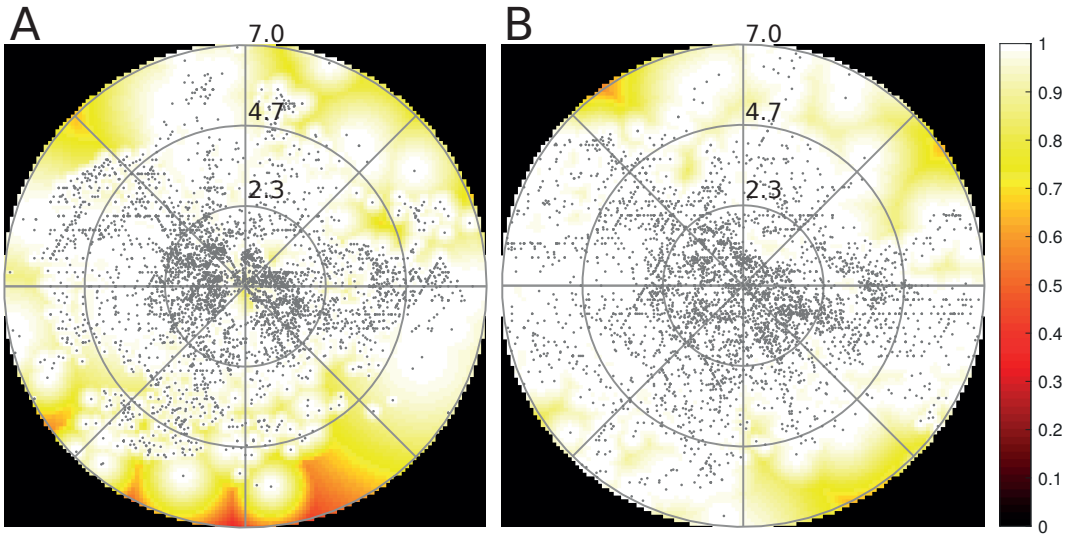

Figure 5.2: Coverage map results from A "wedges and rings" and B "travelling bar" stimuli runs of one typical subject. Thresholds were set to 10 % variance explained.

mapped to the posterior part of V1, estimated pRF size rises with eccentricity, polar angle values associated with the horizontal meridian of the visual field are represented on the contralateral calcarine sulcus while values associated with the vertical meridian indicate the borders of V1 and V2.

When comparing the first two columns, the "wedges and rings" stimulus shows more above-threshold voxels on the occipital pole, compared to the "travelling bar stimulus, which shows improved performance in more peripheral areas. Further extending the comparison to the introduced combination method based on maximum explained variance, the results improve remarkably. In Figure 5.3 the right columns labelled with "MaxVarExp" represent results of the runs being combined by choosing the pRF model with the highest variance explained in every voxel. While A is based on the concatenated "Bar" and "wedges and rings" runs, every run was analysed separately in B. In this exemplary subject, it is shown that the strengths of the single stimuli can be combined, using the proposed method, as the combination has the "wedges and rings" stimulus' excellent performance in the central visual field as well as homogeneous pRF coverage of the whole visual field as found for the travelling bar stimulus. Naturally, the overall explained variance is enhanced, as seen in the plots of the last row.

The visual field coverage maps, averaged from all ten subjects as seen in Figure 5.4 are showing the same patterns as expected from our exemplary subject. The two plots on top

Die approbierte gedruckte Originalversion dieser Diplomarbeit ist an der TU Wien Bibliothek verfügbar.
The approved original version of this thesis is available in print at TU Wien Bibliothek.
TU Bibliothek Your knowledge hub WIEN

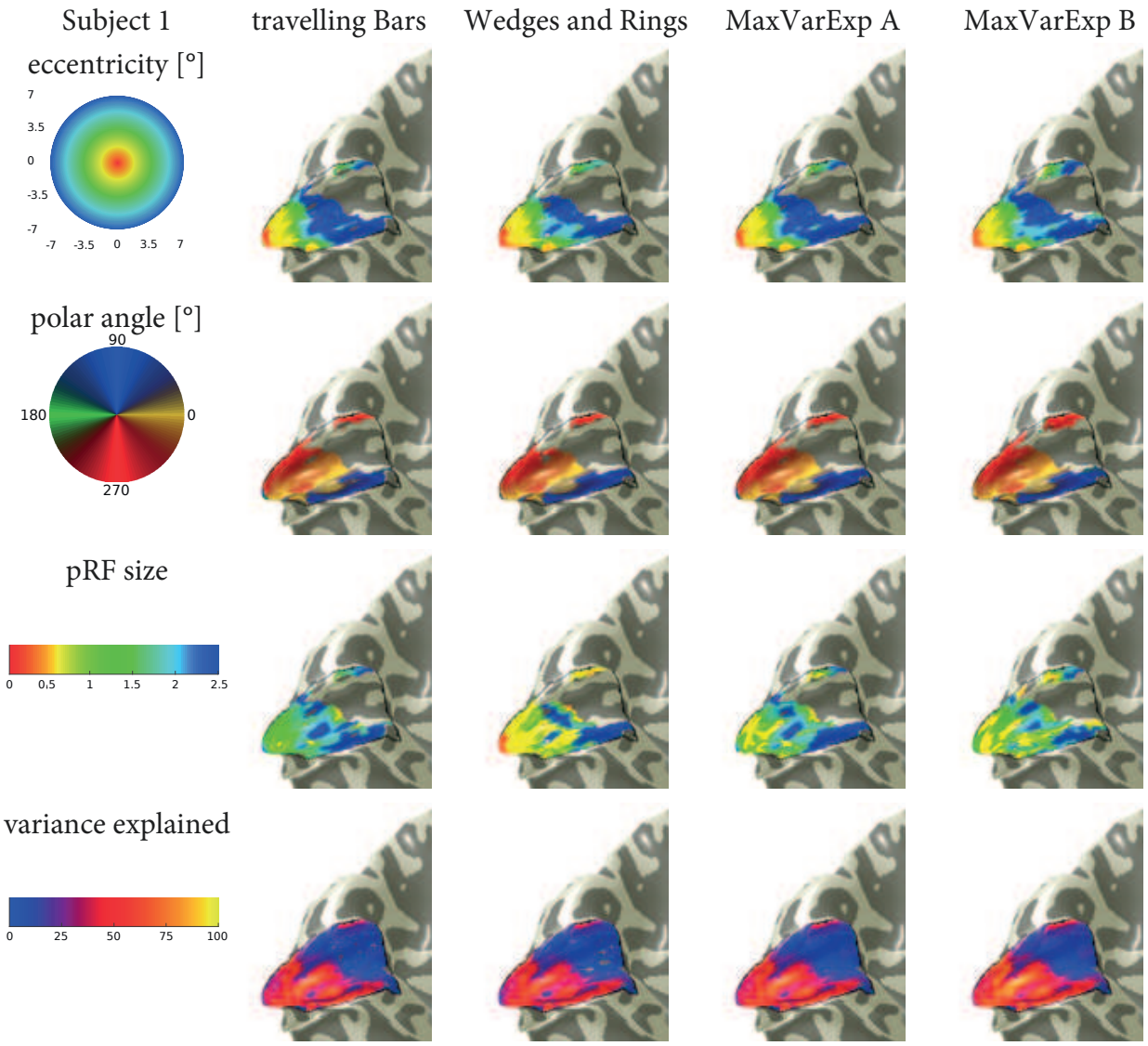

(a) Subject 1

Figure 5.3: The fitting results of one subject are shown, followed by the other single-subject results on the following pages. While the first column shows the respective colour maps for each row, the other columns show estimated pRF parameter maps of different stimuli combination methods. The colour maps for the eccentricity and the polar angle maps are represented in the subject's visual field. The "travelling bar" and "wedges and rings" columns refer to the concatenation of two runs, while the "MaxVarExp" results of each voxel are based on the pRF model showing maximum explained variance. A refers to the combination of the two concatenated "Bar" and "wedges and rings" runs, while the results in B are based on the combination of all four runs analysed separately. The variance explained threshold for the eccentricity, polar angle and pRF size maps are set to 10 %.

Die approbierte gedruckte Originalversion dieser Diplomarbeit ist an der TU Wien Bibliothek verfügbar.
The approved original version of this thesis is available in print at TU Wien Bibliothek.
TU Bibliothek Your knowledge hub WIEN

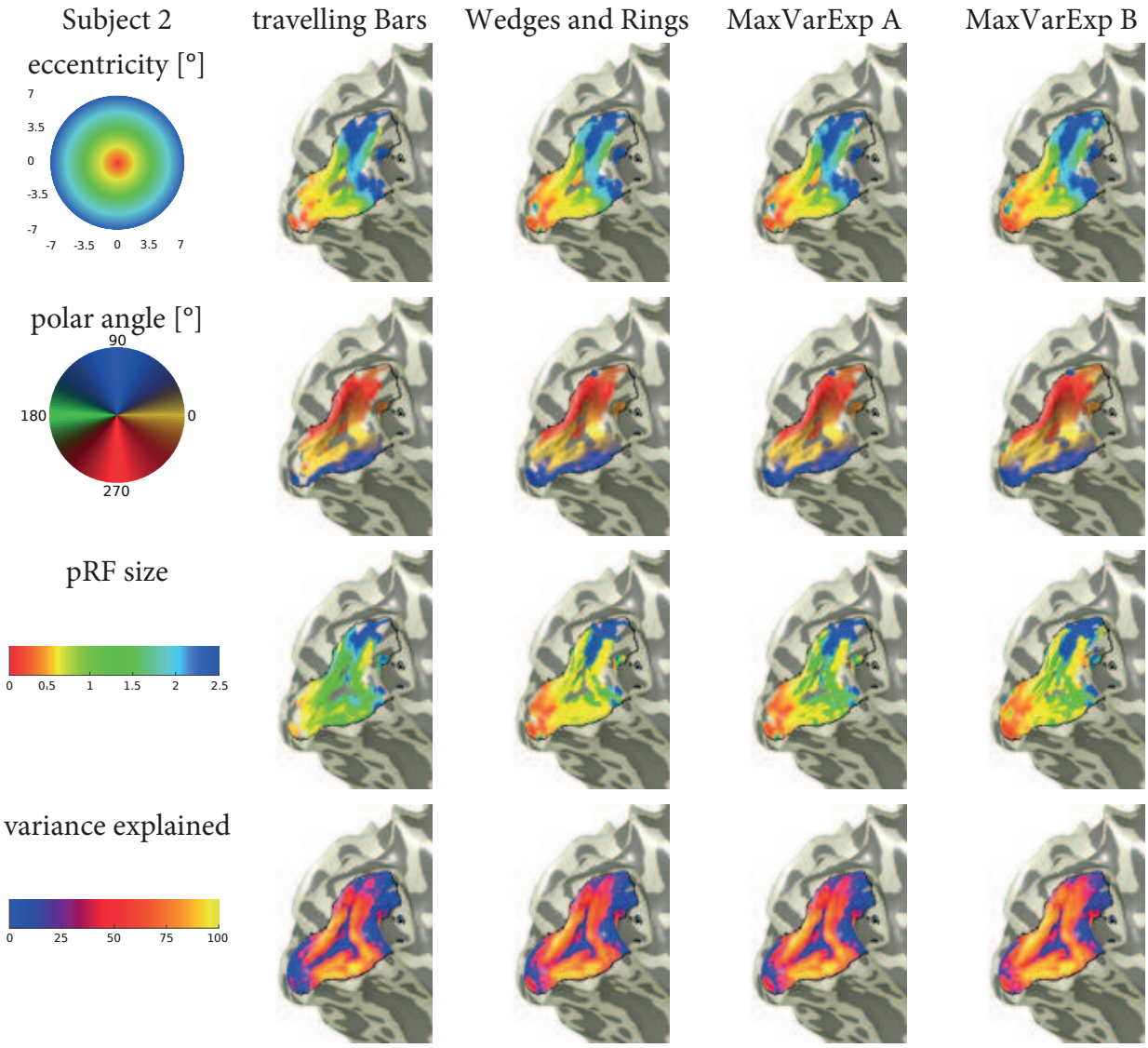

(b) Subject 2

Die approbierte gedruckte Originalversion dieser Diplomarbeit ist an der TU Wien Bibliothek verfügbar.
The approved original version of this thesis is available in print at TU Wien Bibliothek.
TU Bibliothek Your knowledge hub WIEN

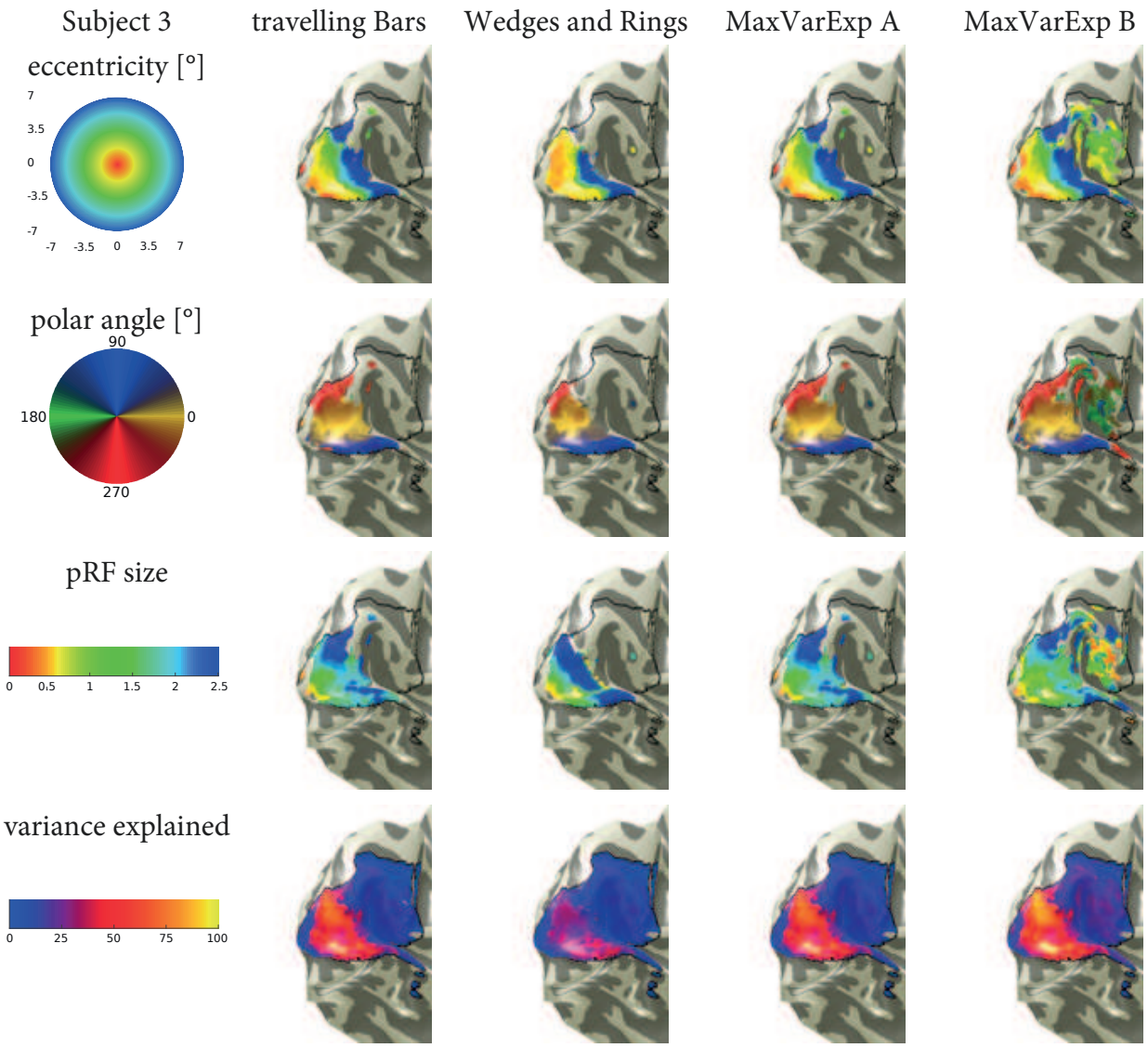

(c) Subject 3

Die approbierte gedruckte Originalversion dieser Diplomarbeit ist an der TU Wien Bibliothek verfügbar.
The approved original version of this thesis is available in print at TU Wien Bibliothek.
TU Bibliothek Your knowledge hub WIEN

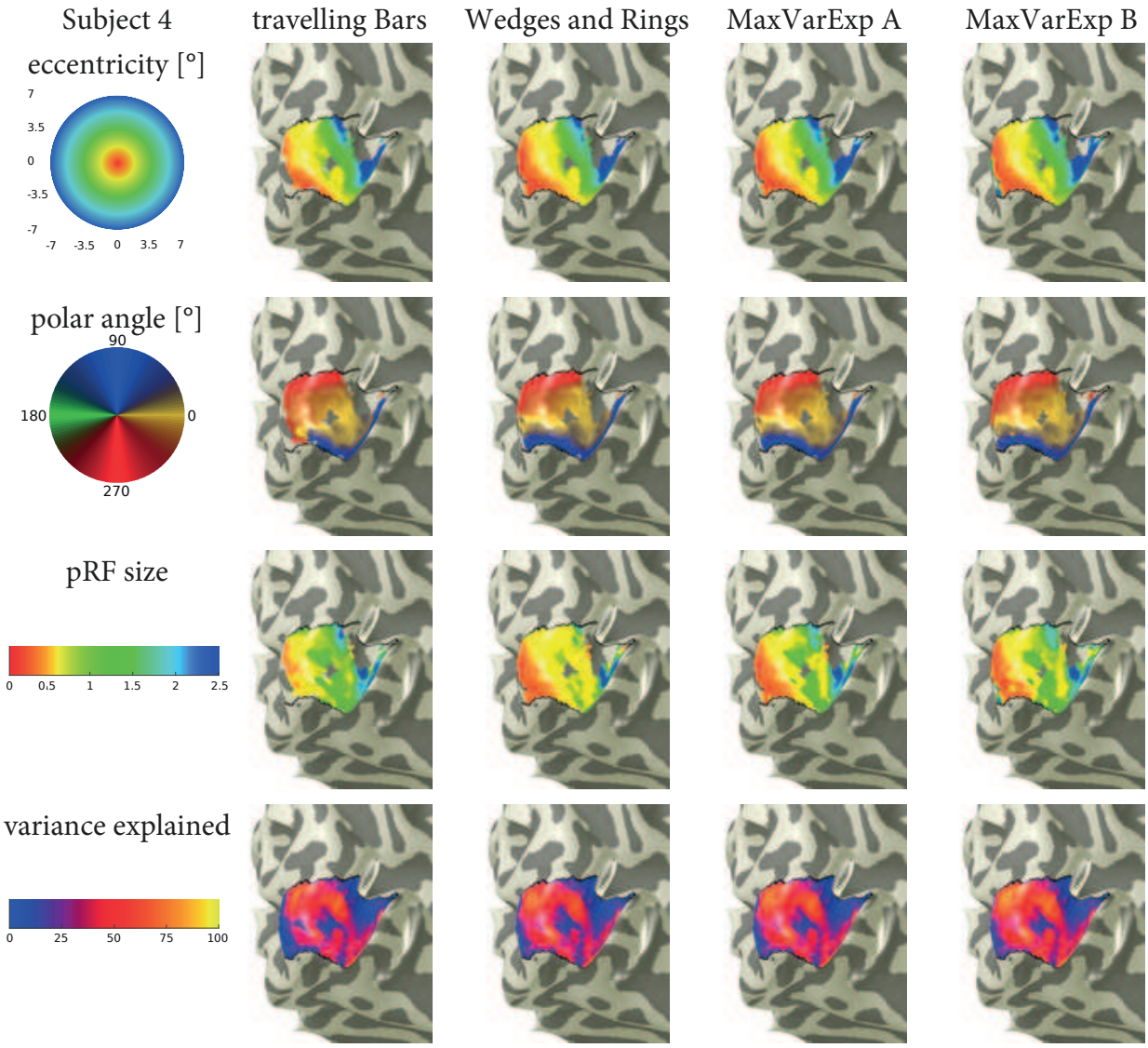

(d) Subject 4

Die approbierte gedruckte Originalversion dieser Diplomarbeit ist an der TU Wien Bibliothek verfügbar.
The approved original version of this thesis is available in print at TU Wien Bibliothek.
TU Bibliothek Your knowledge hub WIEN

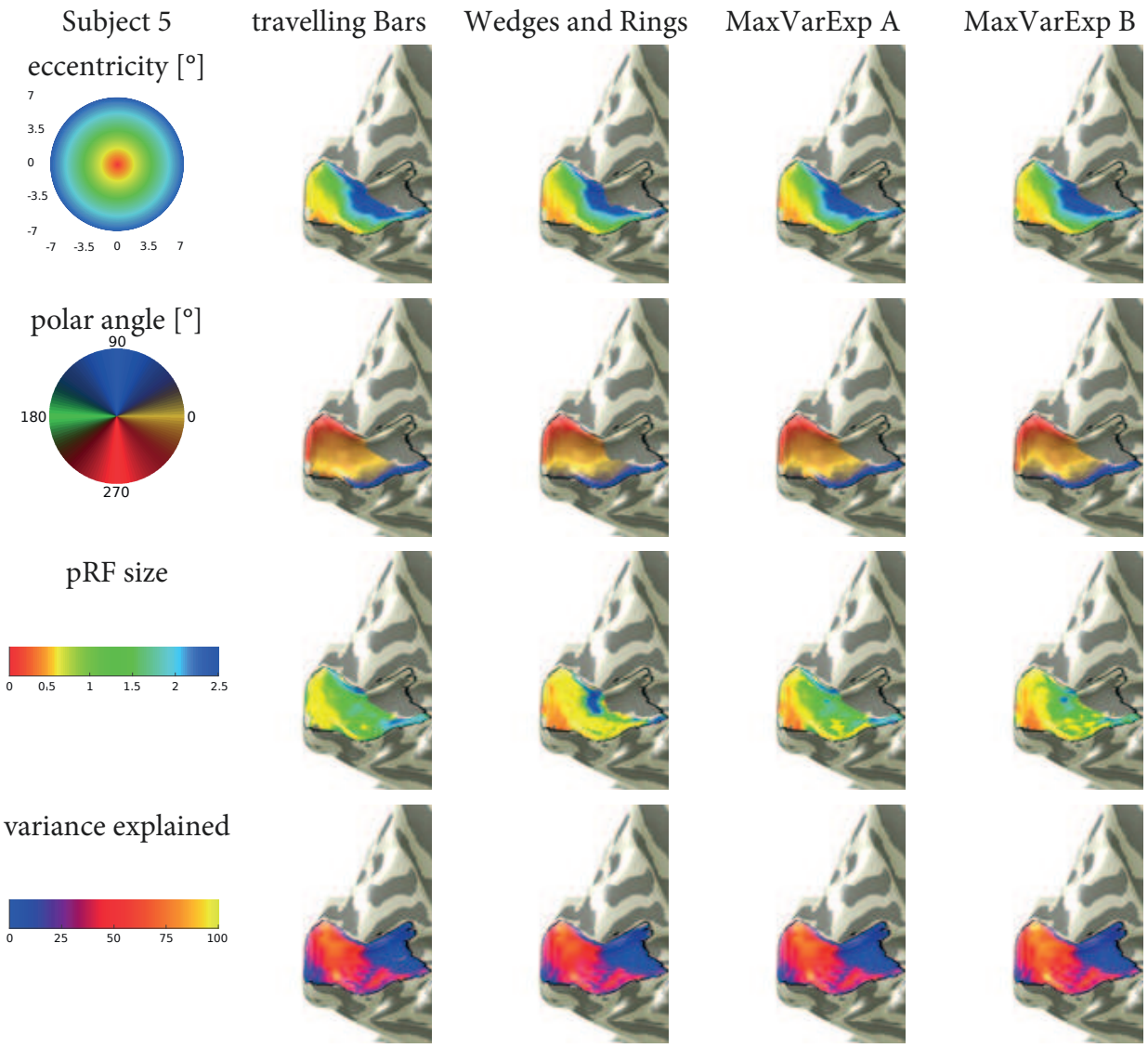

(e) Subject 5

Die approbierte gedruckte Originalversion dieser Diplomarbeit ist an der TU Wien Bibliothek verfügbar.
The approved original version of this thesis is available in print at TU Wien Bibliothek.
TU Bibliothek Your knowledge hub WIEN

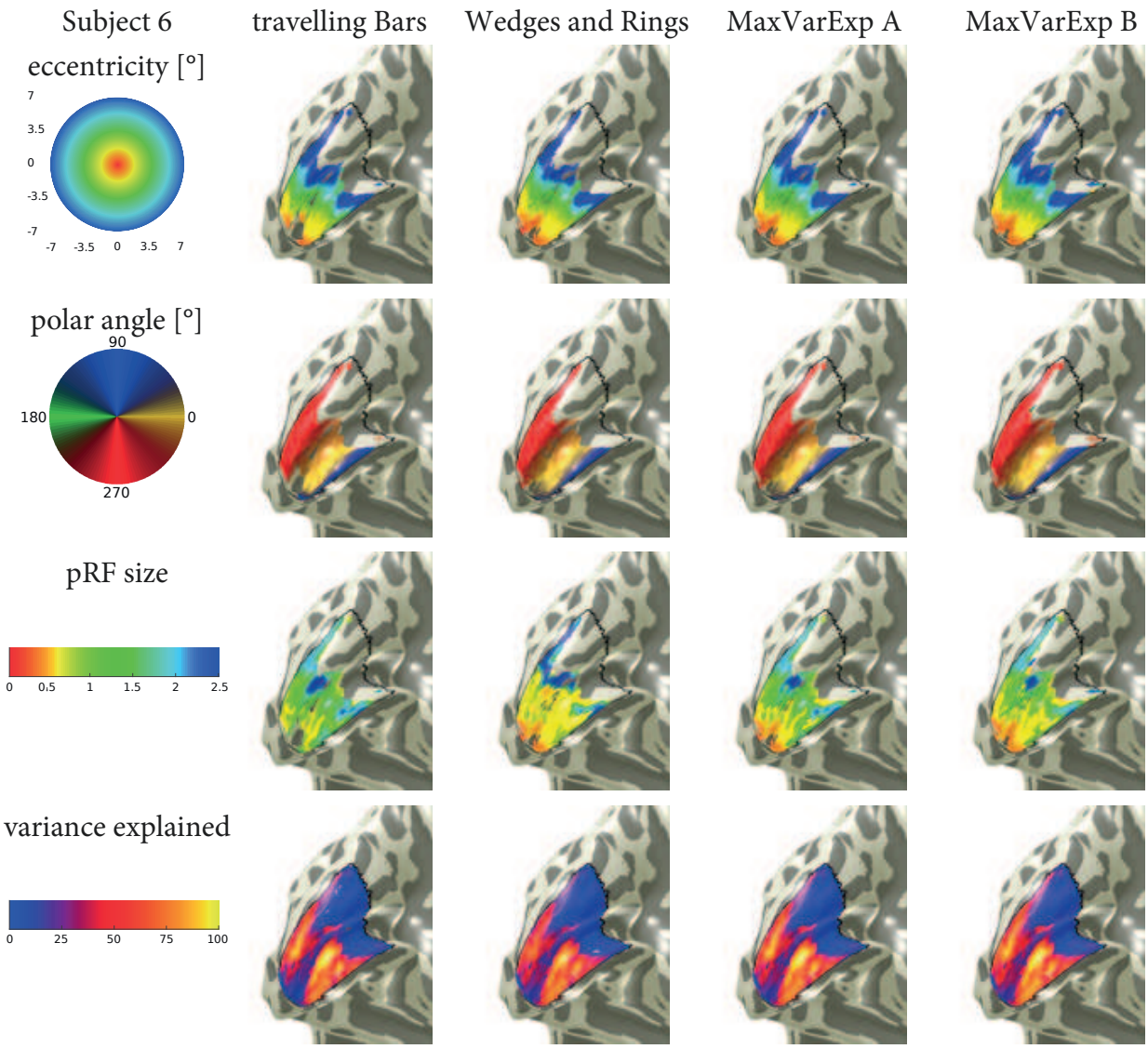

(f) Subject 6

Die approbierte gedruckte Originalversion dieser Diplomarbeit ist an der TU Wien Bibliothek verfügbar.
The approved original version of this thesis is available in print at TU Wien Bibliothek.
TU Bibliothek Your knowledge hub WIEN

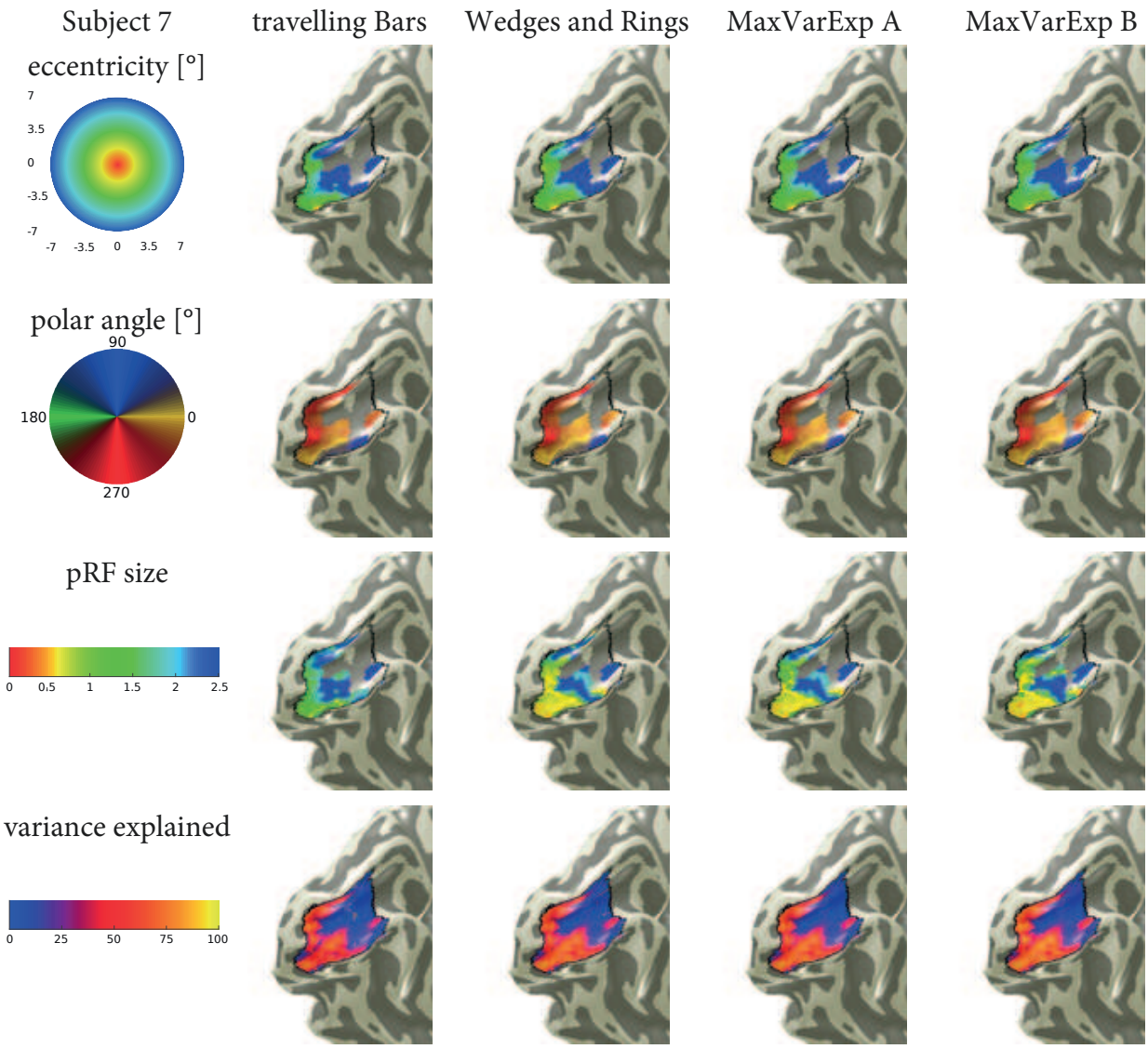

(g) Subject 7

Die approbierte gedruckte Originalversion dieser Diplomarbeit ist an der TU Wien Bibliothek verfügbar.
The approved original version of this thesis is available in print at TU Wien Bibliothek.
TU Bibliothek Your knowledge hub WIEN

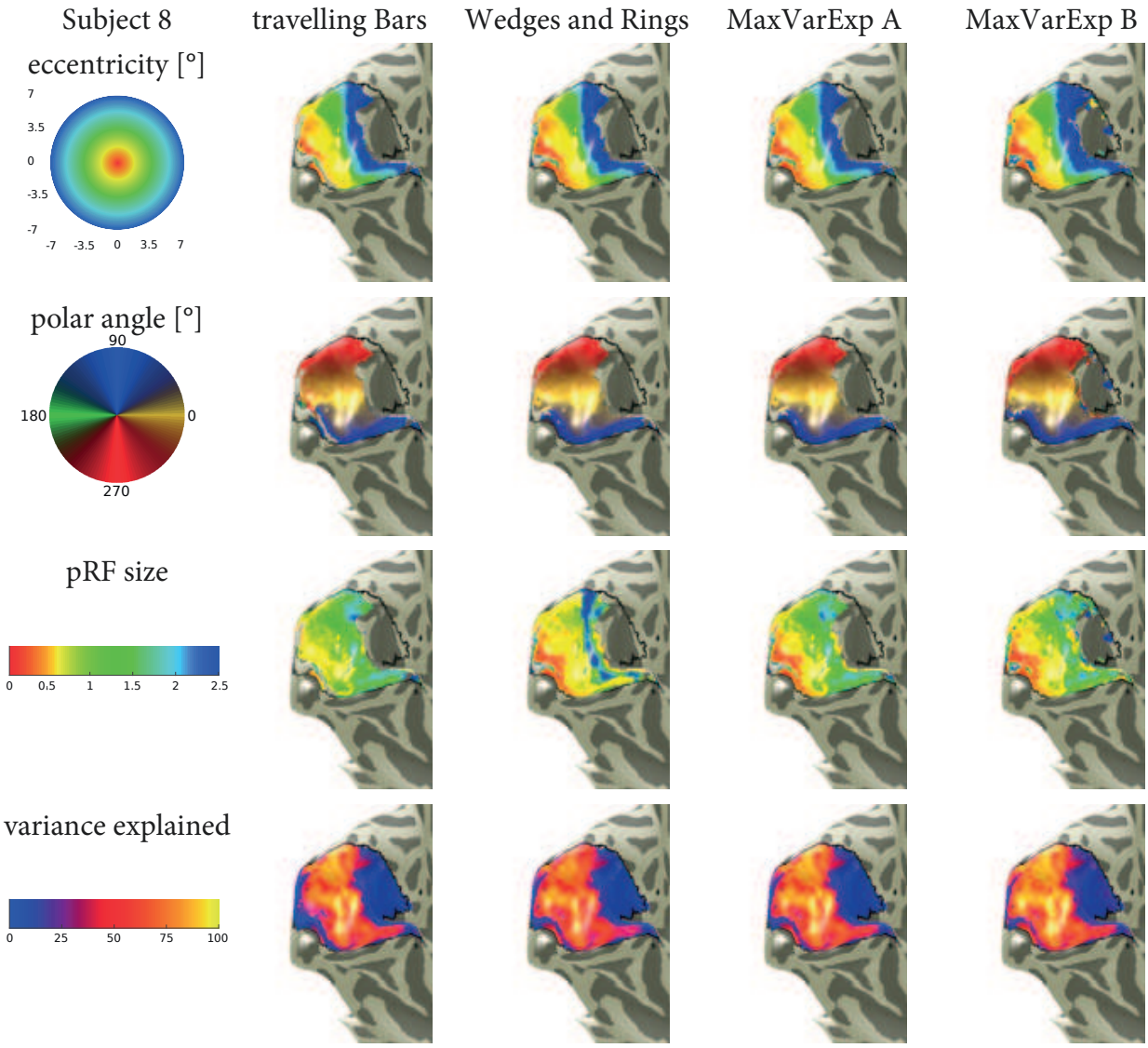

(h) Subject 8

Die approbierte gedruckte Originalversion dieser Diplomarbeit ist an der TU Wien Bibliothek verfügbar.
The approved original version of this thesis is available in print at TU Wien Bibliothek.
TU Bibliothek Your knowledge hub WIEN

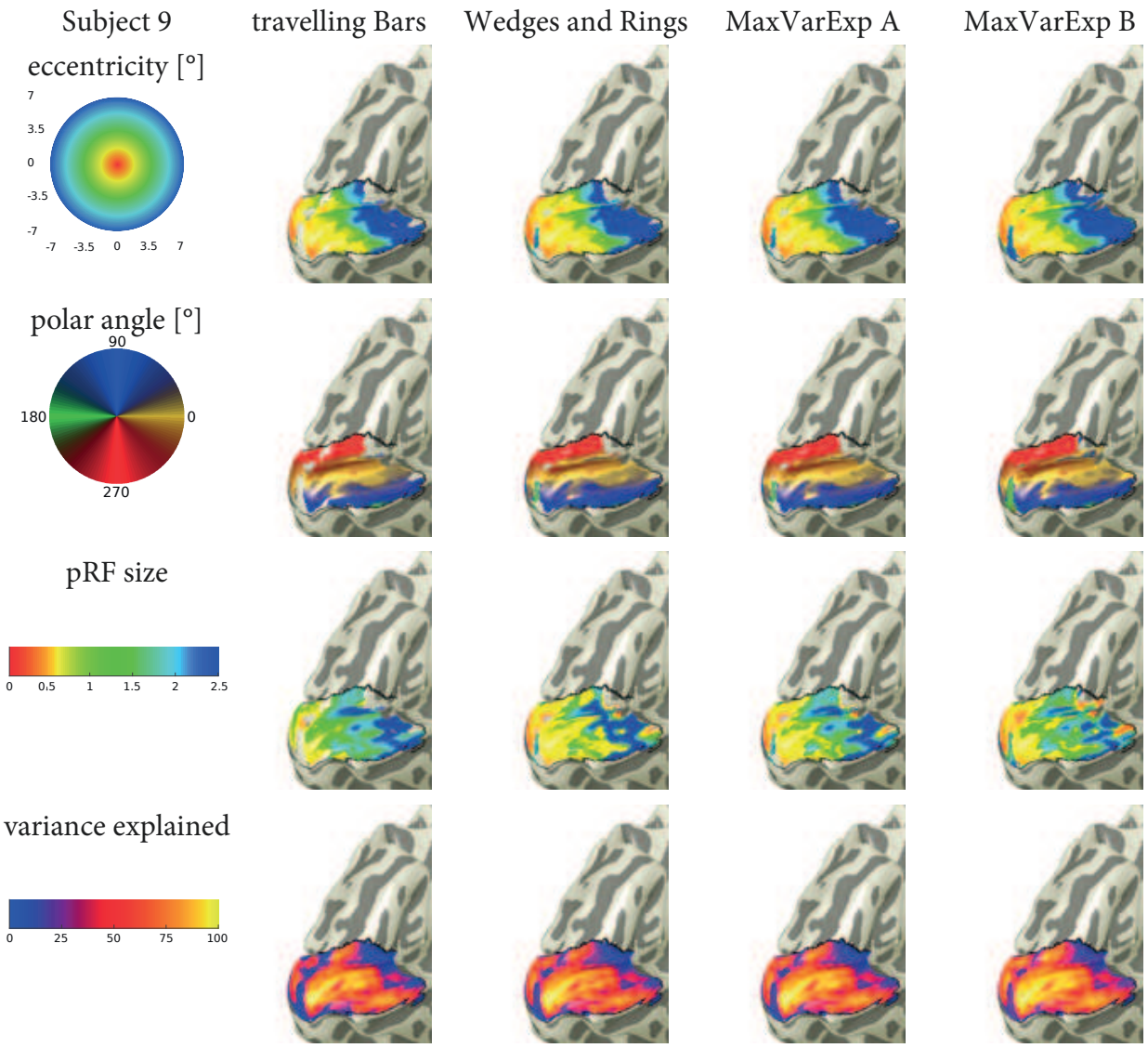

(i) Subject 9

Die approbierte gedruckte Originalversion dieser Diplomarbeit ist an der TU Wien Bibliothek verfügbar.
The approved original version of this thesis is available in print at TU Wien Bibliothek.
TU Bibliothek Your knowledge hub WIEN

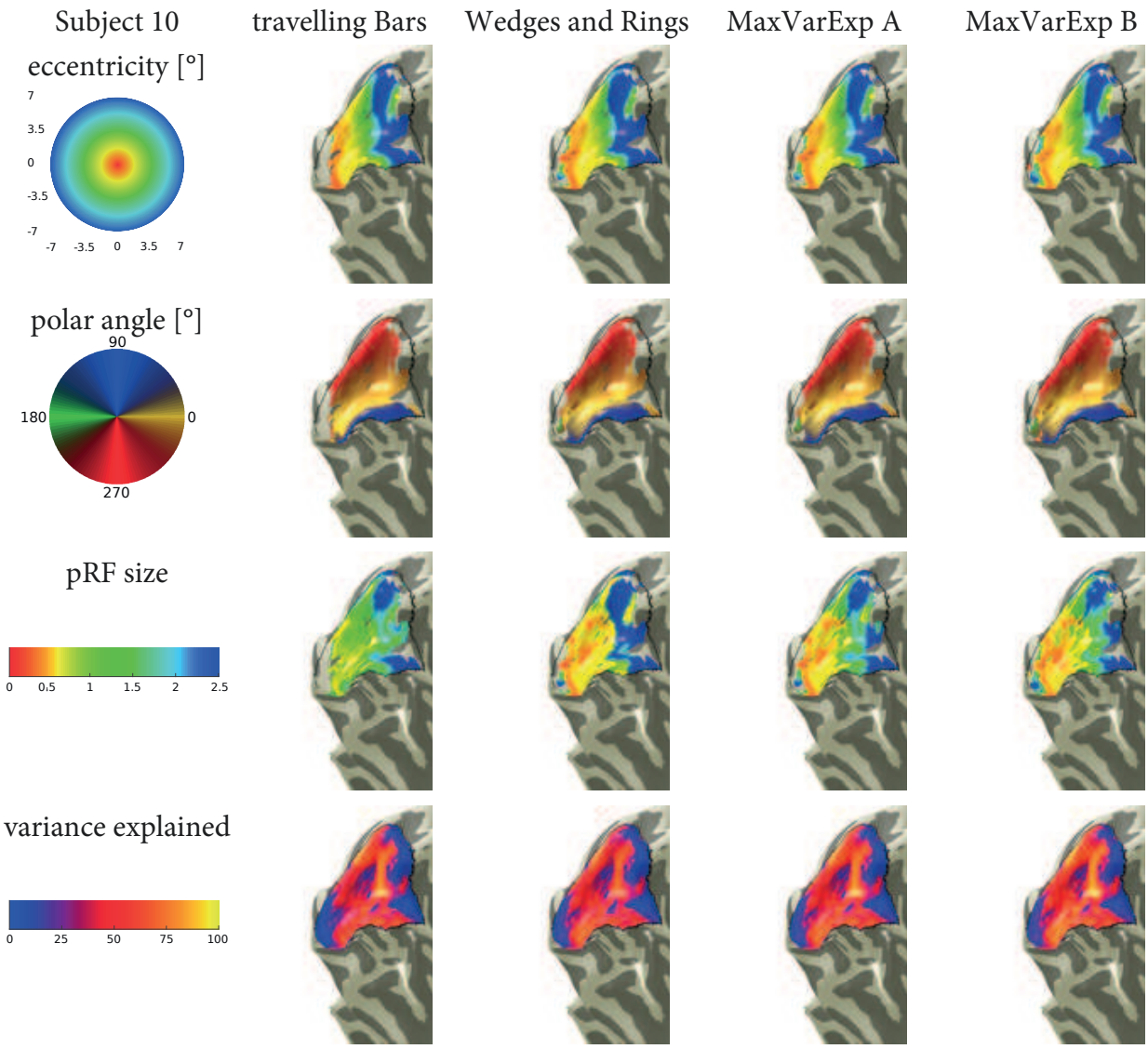

(j) Subject 10

Die approbierte gedruckte Originalversion dieser Diplomarbeit ist an der TU Wien Bibliothek verfügbar.
The approved original version of this thesis is available in print at TU Wien Bibliothek.
TU Bibliothek Your knowledge hub WIEN

Table 5.1: Results for the number of above-threshold voxels and coverage plot mean values averaged across all subjects.

stimulus	voxels	coverage plot mean
travelling bar	10035±1454	0.981±0.021
wedges and rings	10460±1919	0.964±0.031
MaxVarExp A	10893±1702	0.982±0.016
MaxVarExp B	12308±1977	0.993±0.006

Table 5.2: p values, resulting from a paired t-test. The values represent the significance of the increase in above-threshold voxels from the single stimulus (row) to the combined stimulus (column).

	MaxVarExp A	MaxVarExp B
travelling bar	0.00016	0.00021
wedges and rings	0.02045	0.00628

represent the single stimulus analyses, while the two bottom plots represent the combination from the different basis analyses, as described above. In these maps, the different stimuli show specific deficiencies regarding pRF coverage uniformity. While the "travelling bar" stimulus shows an area in the upper part of the visual field which is not well covered consistently over all subjects, the "wedges and rings" stimulus shows a similar area on the bottom part. The combination "MarVarExp A" shows significant improvements in the overall coverage, especially in the problematic parts of the separate analyses, which mostly disappear. However, the combination in "MarVarExp B", based on individual runs, shows an even more uniform coverage over the whole visual field.

Averaged across all ten subjects, the number of voxels above the 10 % variance-explained threshold shows statistically significant increases when the two stimuli are combined as it is shown in Table 5.1, with the significance values in Table 5.2 obtained from a paired t-test comparing the single stimulus and the combination result. Further, the increased homogeneity of the visual field coverage plots is shown by calculating the plot's mean and standard deviation.

Die approbierte gedruckte Originalversion dieser Diplomarbeit ist an der TU Wien Bibliothek verfügbar.
The approved original version of this thesis is available in print at TU Wien Bibliothek.
TU Bibliothek Your knowledge hub WIEN

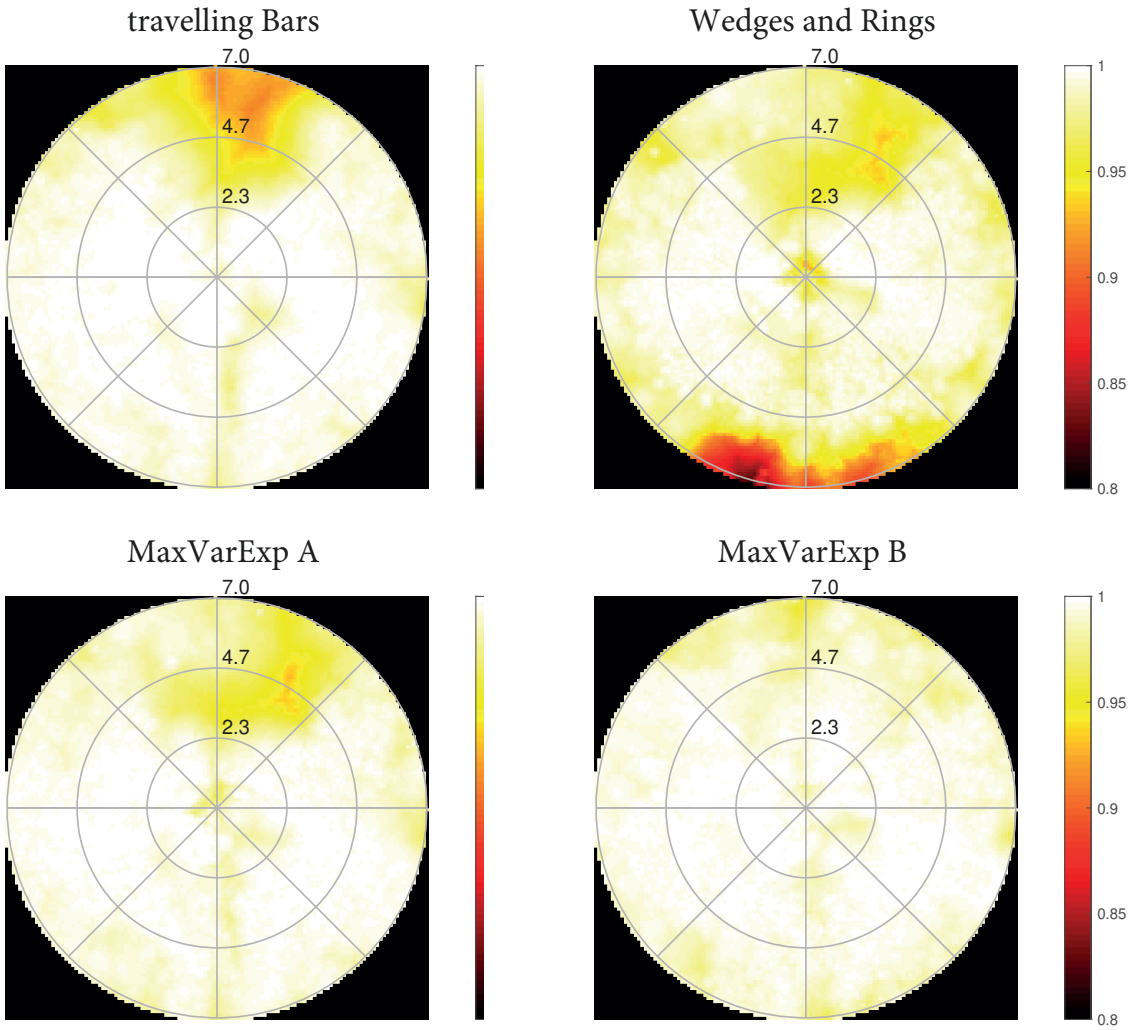

Figure 5.4: Visual field coverage plots were first created for every subject, and combination method individually and afterwards averaged over all ten subjects, illustrating stimulus-specific pRF coverage inhomogeneities.

5.5 Discussion

This study describes and compares the effects of different retinotopic stimuli on pRF parameter estimates and the resulting coverage maps.

The pRF analyses result from ten measured subjects showed the expected eccentricity, polar angle and pRF size maps on the visual cortex. Visual field coverage was found

Die approbierte gedruckte Originalversion dieser Diplomarbeit ist an der TU Wien Bibliothek verfügbar.
The approved original version of this thesis is available in print at TU Wien Bibliothek.
TU Bibliothek Your knowledge hub WIEN

uniform (5.1) which is not surprising since, in healthy, young subjects, continuous attention and excellent fixation stability can be assumed. However, when comparing stimulus-specific results differences in the results obtained from "travelling bar" and "wedges and rings" runs emerge. For a threshold of 10 % explained the variance, the "wedges and rings" runs show more above-threshold voxels in central regions compared to the "travelling bar" stimulus. This may arise from the fact that the bars do not change in thickness or speed depending on their position, and therefore cover the visual field of view very uniformly, while wedges' width depends on eccentricity. Wedges stimulate only small areas in the central visual field at each time point and are thus expected to show more precise results in this area. Following this argument, wedges cover a much larger area in the more peripheral visual field and hence, are expected to perform slightly worse in these regions.

In order to ensure that these observed phenomena are not just subject-specific artefacts caused, for example by movement, the coverage maps from all ten subjects were averaged for both stimuli and showed stimulus-specific shortcomings in several regions of the visual field for both stimuli. While the "travelling bar" stimulus shows areas of decreased coverage in the upper part of the visual field, the "wedges and rings" stimulus shows problems on the bottom. These sections of the visual field are corresponding to the borders of the primary visual cortex, where draining veins could interfere with or even cancel out the BOLD signal [41]. This may not be the central problem here since the venous effects are stable across stimulus variants, and therefore, both stimuli types should suffer equally from these artefacts.

As a proposed solution for these outcomes, a new method for combination of the different stimuli was introduced in order to merge their advantages and compensate for specific problems. Two variants were calculated, first based on the concatenated stimulus-specific runs were combined, and second, all four individual runs were analysed independently and afterwards combined. Variant B, based on the individual runs, seems to yield the best results and therefore, the most uniform coverage of the visual field across all subjects.

In Table 5.1 and Table 5.2 it is shown that the number of above-threshold voxels increases highly significant from the "travelling bar" to both combination methods. Also, from the "wedges and rings" stimulus the number of voxels increases significantly. In Table 5.1 the mean value of the averaged coverage plots is shown where a higher mean value can be interpreted as a higher visual field coverage, while a lower standard devia-

Die approbierte gedruckte Originalversion dieser Diplomarbeit ist an der TU Wien Bibliothek verfügbar.
The approved original version of this thesis is available in print at TU Wien Bibliothek.
TU Bibliothek Your knowledge hub WIEN

tion indicates more homogeneous coverages. The combination coverage plots yield both improved results over the single-stimuli methods. Overall, it can be seen that the second combination method yields even higher significance levels, as well as higher and more homogenous coverage plots.

As demonstrated, better than single-stimulus results can be obtained using combinations of stimuli, mainly used for pRF based retinotopy. However, these stimuli are used, more for historical reasons, rather than because of their proven optimal visual field sampling. Several publications suggest other variants of these stimuli or significantly other approaches like scaled bar stimuli, where the thickness changes logarithmically with the eccentricity [26]. There small advantages of an simultaneous wedges and rings stimulus over the bar stimulus are shown.

Further, so called multifocal stimuli, where segments of the visual field are randomly stimulated are introduced [23]. This multifocal approaches, promise completely decorrelated voxel time-courses and therefore appear as optimal stimuli for retinotopy [42]. However, they lack in explanatory power [39] and result in poorer variance explained [43].

All stimulus comparisons are heavily influenced by non-controllable circumstances like subject attention or movement. Therefore, further research should establish a theoretical framework for the classification of retinotopic stimuli, in order to rate stimuli more objectively and further enable the design of optimal stimuli for the sampling of specific visual field regions.

Die approbierte gedruckte Originalversion dieser Diplomarbeit ist an der TU Wien Bibliothek verfügbar.
The approved original version of this thesis is available in print at TU Wien Bibliothek.
TU Bibliothek Your knowledge hub WIEN

6 Conclusion

In the present study visual cortex data of ten young, healthy subjects were acquired on a 7T Siemens MAGNETOM MRI scanner while presenting two different retinotopic stimuli to the participants. The aim of the thesis was to compare the pRF mapping performance based on the two most commonly used retinotopic mapping visual stimuli, namely "travelling bar" and "wedges and rings". Furthermore, a new stimulus combination method for the enhancement of visual field coverage maps was introduced and tested.

Visible differences in the stimulus-specific performance of the analysis were seen on thresholded cortex maps. Even on the visual field coverage maps averaged over all subjects, areas were heterogeneously covered with regard to visual stimulus variant. Therefore, poorly covered visual field areas were stimulus-specific, which is why problems during the data acquisition and processing can be ruled out. The introduced combination method combines the two presented stimuli voxel-wise and therefore yields much higher overall variance explained and significantly more super-threshold voxels, resulting in more uniform coverage maps, without stimulus-specific problems.

However, the combination of stimuli is no replacement for the discussion about the optimal stimulus. Therefore, the next step will be to establish a simulation framework in order to allow for objective evaluation of visual stimulus performance. This will be achieved by simulation of the specific stimuli's BOLD activation patterns and the subsequent analysis process. In the second step, the framework will be used for optimizing the used stimulus variants and further creating new stimuli. These optimizations will subsequently verified by test measurements.

At 7T stable fixation could not be monitored directly until now. This is not as crucial in healthy subjects, where stable gaze fixation can be expected, as it is in patients suffering from retinal diseases resulting in different forms of visual field losses as fixation performance of these subjects is naturally diminished. In order to monitor and correct for

Die approbierte gedruckte Originalversion dieser Diplomarbeit ist an der TU Wien Bibliothek verfügbar.
The approved original version of this thesis is available in print at TU Wien Bibliothek.
TU Bibliothek Your knowledge hub WIEN

unstable fixation in these populations an eye-tracking system will be installed at the 7T scanner. However, this installation poses various challenges. One of them are the spatial limitations inside the 7T scanner, especially when using the standard 32-channel head coil.

Die approbierte gedruckte Originalversion dieser Diplomarbeit ist an der TU Wien Bibliothek verfügbar.
The approved original version of this thesis is available in print at TU Wien Bibliothek.
TU Bibliothek Your knowledge hub WIEN

Bibliography

1. S. A. Engel, D. E. Rumelhart, B. A. Wandell, A. T. Lee, G. H. Glover, E. J. Chichilnisky, and M. N. Shadlen. "fMRI of human visual cortex". *Nature* 369, 1994, p. 525.

2. S. O. Dumoulin and B. A. Wandell. "Population receptive field estimates in human visual cortex". *NeuroImage* 39:2, 2008, pp. 647 –660. ISSN: 1053-8119. DOI: https://doi.org/10.1016/j.neuroimage.2007.09.034. URL: http://www.sciencedirect.com/science/article/pii/S1053811907008269.

3. P. C. LAUTERBUR. "Image Formation by Induced Local Interactions: Examples Employing Nuclear Magnetic Resonance". *Clinical Orthopaedics and Related Research* 244, 1989. DOI: 10.1038/242190a0.

4. P Mansfield and P. K. Grannell. "NMR 'diffraction' in solids?" *Journal of Physics C: Solid State Physics* 6:22, 1973, pp. L422–L426. DOI: 10.1088/0022-3719/6/22/007. URL: https://doi.org/10.1088%2F0022-3719%2F6%2F22%2F007.

5. F. Bloch, W. W. Hansen, and M. Packard. "Nuclear Induction". *Phys. Rev.* 69, 3-4 1946, pp. 127–127. DOI: 10.1103/PhysRev.69.127. URL: https://link.aps.org/doi/10.1103/PhysRev.69.127.

6. E. M. Purcell, H. C. Torrey, and R. V. Pound. "Resonance Absorption by Nuclear Magnetic Moments in a Solid". *Phys. Rev.* 69, 1-2 1946, pp. 37–38. DOI: 10.1103/PhysRev.69.37. URL: https://link.aps.org/doi/10.1103/PhysRev.69.37.

7. S Ogawa, T. M. Lee, A. R. Kay, and D. W. Tank. "Brain magnetic resonance imaging with contrast dependent on blood oxygenation". *Proceedings of the National Academy of Sciences* 87:24, 1990, pp. 9868–9872. DOI: 10.1073/pnas.87.24.9868. eprint: https://www.pnas.org/content/87/24/9868.full.pdf. URL: https://www.pnas.org/content/87/24/9868.

Die approbierte gedruckte Originalversion dieser Diplomarbeit ist an der TU Wien Bibliothek verfügbar.
The approved original version of this thesis is available in print at TU Wien Bibliothek.
TU Bibliothek Your knowledge hub WIEN

8. R. W. Brown. *Magnetic resonance imaging*. Second edition. Wiley Blackwell, Hoboken, NJ. ISBN: 9781118633953; 9781118633984; 9780471720850.

9. A. Mosso. "Ueber den Kreislauf des Blutes im menschlichen Gehirn.", 1881. URL: https://books.google.at/books?id=6BA_AAAAYAAJ.

10. *Structure of Haemoglobin*. [Online; accessed 20-January-2020]. URL: https://commons.wikimedia.org/wiki/File:Heme_b.svg#/media/File:Heme_b.svg.

11. *k-space EPI acquisition*. [Online; accessed 06-December-2019]. URL: http://mriquestions.com/uploads/3/4/5/7/34572113/4287318_orig.png.

12. K. Eckstein, B. Dymerska, B. Bachrata, W. Bogner, K. Poljanc, S. Trattnig, and S. D. Robinson. "Computationally Efficient Combination of Multi-channel Phase Data From Multi-echo Acquisitions (ASPIRE)". *Magnetic Resonance in Medicine* 79:6, pp. 2996–3006. DOI: 10.1002/mrm.26963. eprint: https://onlinelibrary.wiley.com/doi/pdf/10.1002/mrm.26963. URL: https://onlinelibrary.wiley.com/doi/abs/10.1002/mrm.26963.

13. J. L.R. Andersson, S. Skare, and J. Ashburner. "How to correct susceptibility distortions in spin-echo echo-planar images: Application to diffusion tensor imaging". 20, 2003, pp. 870–88.

14. S. M Smith, M. Jenkinson, M. W Woolrich, C. F Beckmann, T. E J Behrens, H. Johansen-Berg, P. Bannister, M. De Luca, I. Drobnjak, D. Flitney, R. Niazy, J. Saunders, J. Vickers, Y. Zhang, N. De Stefano, M. Brady, and P. Matthews. "Advances in functional and structural MR image analysis and implementation as FSL". 23 Suppl 1, 2004, S208–19.

15. B. A. Wandell. *Foundations of Vision*. 1995.

16. *Anatomy of the human eye*. [Online; accessed 22-January-2020]. URL: https://commons.wikimedia.org/wiki/File:Blausen_0389_EyeAnatomy_02.png#/media/File:Blausen_0389_EyeAnatomy_02.png.

17. *Distribution of rods an cones on the retina*. [Online; accessed 22-January-2020]. URL: https://commons.wikimedia.org/wiki/File:Human_photoreceptor_distribution.svg#/media/File:Human_photoreceptor_distribution.svg.

Die approbierte gedruckte Originalversion dieser Diplomarbeit ist an der TU Wien Bibliothek verfügbar.
The approved original version of this thesis is available in print at TU Wien Bibliothek.
TU Bibliothek Your knowledge hub WIEN

18. *Neural Pathway of the Optic Nerve*. [Online; accessed 22-January-2020]. URL: https://commons.wikimedia.org/wiki/File:Neural_pathway_diagram.svg#/media/File:Neural_pathway_diagram.svg.

19. M. Mishkin and L. G. Ungerleider. "Contribution of striate inputs to the visuospatial functions of parieto-preoccipital cortex in monkeys". *Behavioural Brain Research* 6:1, 1982, pp. 57 –77. ISSN: 0166-4328. DOI: https://doi.org/10.1016/0166-4328(82)90081-X. URL: http://www.sciencedirect.com/science/article/pii/016643288290081X.

20. *Anatomy of the human eye*. [Online; accessed 22-January-2020]. URL: https://commons.wikimedia.org/wiki/File:Ventral-dorsal_streams.svg#/media/File:Ventral-dorsal_streams.svg.

21. G. Holmes. "DISTURBANCES OF VISION BY CEREBRAL LESIONS". *British Journal of Ophthalmology* 2:7, 1918, pp. 353–384. ISSN: 0007-1161. DOI: 10.1136/bjo.2.7.353. eprint: https://bjo.bmj.com/content/2/7/353.full.pdf. URL: https://bjo.bmj.com/content/2/7/353.

22. T. Inouye. "Die Sehstorungen bei Schussverletzungen der Kortikalen Sehsphare". *Nach Beobachtungen an Verwundeten der letszten japanischen Kriege.*, 1909. URL: https://ci.nii.ac.jp/naid/10010929493/en/.

23. S. Vanni, L. Henriksson, and A. James. "Multifocal fMRI mapping of visual cortical areas". *NeuroImage* 27:1, 2005, pp. 95 –105. ISSN: 1053-8119. DOI: https://doi.org/10.1016/j.neuroimage.2005.01.046. URL: http://www.sciencedirect.com/science/article/pii/S1053811905000790.

24. N. C. Benson, K. W. Jamison, M. J. Arcaro, A. Vu, M. F. Glasser, T. S. Coalson, D. C. Van Essen, E. Yacoub, K. Ugurbil, J. Winawer, and K. Kay. "The HCP 7T Retinotopy Dataset: Description and pRF Analysis". *bioRxiv*, 2018. DOI: 10.1101/308247. eprint: https://www.biorxiv.org/content/early/2018/08/30/308247.full.pdf. URL: https://www.biorxiv.org/content/early/2018/08/30/308247.

25. A. Hummer, M. Ritter, M. Woletz, A. Ledolter, M. Tik, and C. Windischberger. "Population receptive field coverage provided by different retinotopic stimuli in healthy subjects". *Annual Meeting of the Organization for Human Brain Mapping (OHBM), Singapore, Republic of Singapore*, 2018b.

Die approbierte gedruckte Originalversion dieser Diplomarbeit ist an der TU Wien Bibliothek verfügbar.
The approved original version of this thesis is available in print at TU Wien Bibliothek.
TU Bibliothek Your knowledge hub WIEN

26. I. Alvarez, B. De Haas, C. Clark, G. Rees, and D Schwarzkopf. "Comparing different stimulus configurations for population receptive field mapping in human fMRI". *Frontiers in Human Neuroscience* 9, 2015, p. 96. ISSN: 1662-5161. DOI: 10.3389/fnhum.2015.00096. URL: https://www.frontiersin.org/article/10.3389/fnhum.2015.00096.

27. P. Jezzard and R. S. Balaban. "Correction for geometric distortion in echo planar images from B0 field variations". *Magnetic Resonance in Medicine* 34:1, 1995, pp. 65–73. DOI: 10.1002/mrm.1910340111. eprint: https://onlinelibrary.wiley.com/doi/pdf/10.1002/mrm.1910340111. URL: https://onlinelibrary.wiley.com/doi/abs/10.1002/mrm.1910340111.

28. D. Linhardt. "Distortion Correction at Ultra-high Fields". *Project Thesis*.

29. S. E. HENSCHEN. " ON THE VISUAL PATH AND CENTRE 1". *Brain* 16:1-2, 1893, pp. 170–180. ISSN: 0006-8950. DOI: 10.1093/brain/16.1-2.170. eprint: http://oup.prod.sis.lan/brain/article-pdf/16/1-2/170/6695912/16-1-2-170.pdf. URL: https://doi.org/10.1093/brain/16.1-2.170.

30. J. C. Horton and W. F. Hoyt. "The Representation of the Visual Field in Human Striate Cortex: A Revision of the Classic Holmes Map". *Archives of Ophthalmology* 109:6, 1991, pp. 816–824. ISSN: 0003-9950. DOI: 10.1001/archopht.1991.01080060080030. eprint: https://jamanetwork.com/journals/jamaophthalmology/articlepdf/639114/archopht_109_6_030.pdf. URL: https://doi.org/10.1001/archopht.1991.01080060080030.

31. B. Fischl and A. M. Dale. "Measuring the thickness of the human cerebral cortex from magnetic resonance images". *Proceedings of the National Academy of Sciences* 97:20, 2000, pp. 11050–11055. ISSN: 0027-8424. DOI: 10.1073/pnas.200033797. eprint: https://www.pnas.org/content/97/20/11050.full.pdf. URL: https://www.pnas.org/content/97/20/11050.

32. B. A. Wandell and J. Winawer. "Imaging retinotopic maps in the human brain". *Vision Research* 51, 2011, pp. 718–737.

33. W. Zuiderbaan, B. M. Harvey, and S. O. Dumoulin. "Modeling center–surround configurations in population receptive fields using fMRI". *Journal of Vision* 12:3, 2012, pp. 10–10. ISSN: 1534-7362. DOI: 10.1167/12.3.10. eprint: https://jov.

Die approbierte gedruckte Originalversion dieser Diplomarbeit ist an der TU Wien Bibliothek verfügbar.
The approved original version of this thesis is available in print at TU Wien Bibliothek.
TU Bibliothek Your knowledge hub WIEN

arvojournals.org/arvo/content_public/journal/jov/932803/jov-12-3-10.pdf. URL: https://doi.org/10.1167/12.3.10.

34. E. H. Silson, R. C. Reynolds, D. J. Kravitz, and C. I. Baker. "Differential Sampling of Visual Space in Ventral and Dorsal Early Visual Cortex". *Journal of Neuroscience* 38:9, 2018, pp. 2294–2303. ISSN: 0270-6474. DOI: 10.1523/JNEUROSCI.2717-17.2018. eprint: https://www.jneurosci.org/content/38/9/2294.full.pdf. URL: https://www.jneurosci.org/content/38/9/2294.

35. M. Sereno, A. Dale, J. Reppas, K. Kwong, J. Belliveau, T. Brady, B. Rosen, and R. Tootell. "Borders of multiple visual areas in humans revealed by functional magnetic resonance imaging". *Science* 268:5212, 1995, pp. 889–893. ISSN: 0036-8075. DOI: 10.1126/science.7754376. eprint: https://science.sciencemag.org/content/268/5212/889.full.pdf. URL: https://science.sciencemag.org/content/268/5212/889.

36. E. H. Silson, A. W.-Y. Chan, R. C. Reynolds, D. J. Kravitz, and C. I. Baker. "A Retinotopic Basis for the Division of High-Level Scene Processing between Lateral and Ventral Human Occipitotemporal Cortex". *Journal of Neuroscience* 35:34, 2015, pp. 11921–11935. ISSN: 0270-6474. DOI: 10.1523/JNEUROSCI.0137-15.2015. eprint: https://www.jneurosci.org/content/35/34/11921.full.pdf. URL: https://www.jneurosci.org/content/35/34/11921.

37. J. A. van Dijk, B. de Haas, C. Moutsiana, and D. S. Schwarzkopf. "Intersession reliability of population receptive field estimates". *NeuroImage* 143, 2016, pp. 293 – 303. ISSN: 1053-8119. DOI: https://doi.org/10.1016/j.neuroimage.2016.09.013. URL: http://www.sciencedirect.com/science/article/pii/S105381191630475X.

38. L. E. Welbourne, A. B. Morland, and A. R. Wade. "Population receptive field (pRF) measurements of chromatic responses in human visual cortex using fMRI". *NeuroImage* 167, 2018, pp. 84 –94. ISSN: 1053-8119. DOI: https://doi.org/10.1016/j.neuroimage.2017.11.022. URL: http://www.sciencedirect.com/science/article/pii/S1053811917309291.

39. Y. Ma, B. D. Ward, K. M. Ropella, and E. A. DeYoe. "Comparison of randomized multifocal mapping and temporal phase mapping of visual cortex for clinical use". *NeuroImage: Clinical* 3, 2013, pp. 143 –154. ISSN: 2213-1582. DOI: https://doi.

Die approbierte gedruckte Originalversion dieser Diplomarbeit ist an der TU Wien Bibliothek verfügbar.
The approved original version of this thesis is available in print at TU Wien Bibliothek.
TU Bibliothek Your knowledge hub WIEN

org/10.1016/j.nicl.2013.08.004. URL: http://www.sciencedirect.com/science/article/pii/S2213158213001046.

40. S. Moeller, E. Yacoub, C. A. Olman, E. Auerbach, J. Strupp, N. Harel, and K. Uğurbil. "Multiband multislice GE-EPI at 7 tesla, with 16-fold acceleration using partial parallel imaging with application to high spatial and temporal whole-brain fMRI". *Magnetic Resonance in Medicine* 63:5, 2010, pp. 1144–1153. DOI: 10.1002/mrm.22361. eprint: https://onlinelibrary.wiley.com/doi/pdf/10.1002/mrm.22361. URL: https://onlinelibrary.wiley.com/doi/abs/10.1002/mrm.22361.

41. K. Kay, K. W. Jamison, L. Vizioli, R. Zhang, E. Margalit, and K. Ugurbil. "A critical assessment of data quality and venous effects in ultra-high-resolution fMRI". *bioRxiv*, 2018. DOI: 10.1101/337667. eprint: https://www.biorxiv.org/content/early/2018/06/03/337667.full.pdf. URL: https://www.biorxiv.org/content/early/2018/06/03/337667.

42. G. T. Buračas and G. M. Boynton. "Efficient Design of Event-Related fMRI Experiments Using M-Sequences". *NeuroImage* 16:3, Part A, 2002, pp. 801 –813. ISSN: 1053-8119. DOI: https://doi.org/10.1006/nimg.2002.1116. URL: http://www.sciencedirect.com/science/article/pii/S105381190291116X.

43. P. Binda, J. M. Thomas, G. M. Boynton, and I. Fine. "Minimizing biases in estimating the reorganization of human visual areas with BOLD retinotopic mapping". *Journal of Vision* 13:7, 2013, pp. 13–13. ISSN: 1534-7362. DOI: 10.1167/13.7.13. eprint: https://arvojournals.org/arvo/content_public/journal/jov/932812/i1534-7362-13-7-13.pdf. URL: https://doi.org/10.1167/13.7.13.

Die approbierte gedruckte Originalversion dieser Diplomarbeit ist an der TU Wien Bibliothek verfügbar.
The approved original version of this thesis is available in print at TU Wien Bibliothek.
TU Bibliothek Your knowledge hub WIEN